To the Graduate Council:

I am submitting herewith a thesis written by Joseph Pierre Serge Boudreault entitled "Effect of Nonparallelism on the Measurement of Ultrasonic Attenuation in Solids." I have examined the final copy of this thesis for form and content and recommend that it be accepted in partial fulfillment of the requirements for the degree of Master of Science, with a major in Engineering Science and Mechanics.

M. A. Breazeale, Major Professor

We have read this thesis and recommend its acceptance:

Bruce R Bursey

W. E. Deeds

Accepted for the Council:

L Evans Roth

Vice Chancellor
Graduate Studies and Research

EFFECT OF NONPARALLELISM ON THE MEASUREMENT OF ULTRASONIC ATTENUATION IN SOLIDS

A Thesis

Presented for the

Master of Science

Degree

The University of Tennessee, Knoxville

Joseph Pierre Serge Boudreault

August 1982

3063063

Dédicace

à Line

Merci

Pour ces heures supplémentaires
Que tu as passé
A compenser
Pour mon trop à faire.

Pour être malgré tout demeurée
Une mère exemplaire
Et une douce moitié
Dont tout mari serait fier.

Pour avoir tout accepté
Si gracieusement
Et si simplement,
Que je n'ai pas eu à le demander.

Aucun merci ne pourrait suffire.

Serge

ACKNOWLEDGMENT

The author wishes to acknowledge the contributions of the following organizations:

The Canadian Armed Forces for their financial and administrative support;

The United States Office of Naval Research for providing the equipment, the laboratory space, and for use of the facilities at The University of Tennessee Computing Center;

The Metals and Ceramics Division of Oak Ridge National Laboratory for providing the steel sample and for giving me the opportunity to work on nondestructive applications.

The author also wishes to express his appreciation to a few special individuals. They are:

Dr. M. A. Breazeale for his patience, and his dedication to the task of guiding this work and also for the benevolence shown by him and his family;

Dr. Jacob Philip and Mr. Jerry Latimer for their friendship and many hours spent in giving technical advice;

The personnel of the Ultrasonic Section of the Metals and Ceramics Division of Oak Ridge National Laboratory for their cooperation and genuine interest in helping;

Mrs. Maxine Martin for the expertise and dedication that she has shown in the assembling and typing of the thesis.

ABSTRACT

Evaluation of attenuation of ultrasonic waves in solids from pulse echo trains can be complicated by a number of factors. In this thesis one considers the effect of nonparallelism of the sample surfaces. A mathematical model for correcting the echo height for the effect of a wedge-shaped sample is constructed. By using a unique coordinate system, the path of a multiply-reflected ultrasonic wave is transformed into an equivalent unidirectional path. A diffraction correction then is applied by numerically integrating an improved version of the farfield solution to the diffraction integral. This model is used to interpret data taken on a steel plate which has different facets ground over a range of angles between 0 and 0.01175 radians. Plots are given of corrected attenuation measurements made with circular piezoelectric transucers having resonance frequencies between 3 and 7 MHz.

A comparison is made between the present model and that of Truell and Oates [J. Acoust. Soc. Am. 35, 1382 (1963)], which was intended as an indicator of the necessity for applying a correction for nonparallelism. The present model corrects the first four echoes for frequencies $f < 6$ MHz and angles $\gamma < 4 \times 10^{-3}$ radians.

TABLE OF CONTENTS

CHAPTER		PAGE
I.	INTRODUCTION	1
II.	THEORETICAL ANALYSIS	5
	Wave Propagation Theory	5
	Wave Attenuation	5
	Definition of α, the attenuation parameter	5
	The attenuation correction	6
	The Diffraction Theory	7
	The diffraction model	7
	The pressure on the axis	10
	The pressure in the farfield	12
	Average pressure on the receiver	14
	Geometrical Correction Models	17
	The Plane Wave Correction Model	17
	The geometry of propagation in a wedged sample	17
	The theory of Truell and Oates	19
	The average pressure on the receiver	20
	The Diffracted Wave Model	20
	Model of the physical situation	21
	Modification of the solution of the diffraction integral in the farfield	21
	The coordinate transformations	23
	The average pressure on the receiver	31
	The Correction for Geometrical Attenuation	34
III.	EXPERIMENTAL APPARATUS AND PROCEDURE	36
	Purpose and Background	36
	Experimental Apparatus	36
	Electronic Components	36
	System description	36
	System discussion	38
	Transducer	39
	Structure	39
	Electrical circuit	42
	Sample	43
	Experimental Procedure	45
	Sample Characterization	45
	Angles measurements	45
	Velocity measurement	47
	Attenuation Measurements	50
IV.	RESULTS AND CONCLUSIONS	52
	Experimental Results	52

CHAPTER PAGE

The Amplitude Pattern 52
The Attenuation Parameter 52
The Diffraction Correction 56
Application of the Plane Wave Geometrical Correction . . . 62
Application of the Diffracted Wave Geometrical Correction 65
Conclusions 69
Suggestions for Further Work 71
Receiver Directivity Factor 71
Correction in the Fresnel Zone 72
The Gaussian Transducer Model 72
Velocity Measurements 72

LIST OF REFERENCES 74

APPENDICES 77

A. AN APPLICATION OF THE RECIPROCITY THEOREM 78

B. A COMPUTER PROGRAM FOR CORRECTING ULTRASONIC ATTENUATION DATA 82

C. PHASE CORRECTION FOR VELOCITY MEASUREMENTS 87

D. THE RECEIVER DIRECTIVITY MODEL 91

E. THE GAUSSIAN TRANSDUCER 96

VITA 101

LIST OF FIGURES

FIGURE		PAGE
II-1.	Geometry Used in Deriving the Radiation Characteristics of a Piston Source	9
II-2.	The Shape of the Normalized Values of Pressure in a Plane Normal to the Direction of Propagation (from Mercier (1976))	11
II-3.	Comparison of Pressure on Axis for $P_0 = 1$ (from Krautkramer (1977))	13
II-4.	Functional Behavior of $2J_1(ka \sin\theta)/ka \sin\theta$ (from Kinsler et al. (1982))	15
II-5.	Directional Characteristic $H(\theta)$ (from Krautkramer (1977))	16
II-6.	Propagation Path of the Center of the Disturbance	18
II-7.	Schematic Representation of the Wavefront Showing the Amplitude Distribution and the Relative Source and Receiver Position after n Reflections	22
II-8.	Inverse of the Average Pressure on the Receiver as a Function of Normalized Propagation Distance	24
II-9.	Geometrical Relationship Existing for n = 1	26
II-10.	Graphical Construction Showing the Geometrical Relations after Three Reflections	29
II-11.	Definition of the Receiver Coordinate (x,y) in the $\rho'_n Z'_n$ Plane	30
II-12.	Definition of the Coordinate $[\rho'(x,y)]_n$ in the $\rho'_n \phi'_n$ Plane	32
III-1.	Electronic Circuits Used for Acoustical Measurements	37
III-2.	Ultrasonic Measurement Setup Showing the Steel Plate, the Transducer, and the Vise	40
III-3.	Transducer Parts	41
III-4.	Geometry of the Wedged Sample	44

FIGURE		PAGE
III-5.	Schematic of Optical Measurement Setup	46
IV-1.	Exponential Decay Pattern at 6 MHz for 0 Wedge Angle . . .	53
IV-2.	Fluctuations in the Echo Pattern Observed at 3 MHz for $\gamma = 11.75 \times 10^{-3}$ Radians	54
IV-3.	Pulse Amplitude Pattern at 4 MHz for a Wedge Angle of 11.75×10^{-3} Radians	55
IV-4.	Apparent Attenuation at 4 MHz for Different Wedge Angles	57
IV-5.	Apparent Attenuation at 7 MHz for Different Wedge Angles	58
IV-6.	Attenuation at 3.34 MHz for 0 Wedge Angle	60
IV-7.	Attenuation at 6.00 MHz for 0 Wedge Angle	61
IV-8.	Attenuation at 4 MHz for a Wedge Angle of 11.75×10^{-3} Radians Using the Truell and Oates Correction	64
IV-9.	Attenuation at 4 MHz for a Wedge Angle of 11.75×10^{-3} Radians Using Data Corrected for Diffracted Wave Geometry	66
IV-10.	Attenuation at 5.75 MHz for a Wedge Angle of 3.82×10^{-3} Radians Using Data Corrected for Diffracted Wave Geometry and Reference Attenuation for $\gamma = 0$ and $f = 6$ MHz	67
IV-11.	Attenuation at 3.31 MHz for a Wedge Angle of 3.82×10^{-3} Radians Using Data Corrected for Diffracted Wave Geometry and Reference Attenuation for $\gamma = 0$ and $f = 3.34$ MHz . . .	68
A-1.	Theoretical Position of Two Transducers Enclosed in a Volume V	79
D-1.	Schematic Showing the Relative Position of the Transducers S_1 and S_2 and the Incident Angle θ of the Incoming Plane Wave	93
D-2.	Schematic Showing the Relation between Two Transducers S_1 and S_2 which Have Parallel Acoustic Axes	95

CHAPTER I

INTRODUCTION

The attenuation of ultrasonic waves is a physical phenomenon which has great significance in many wave propagation studies. Much useful information about the internal structure of the propagating medium can be derived from a correct interpretation of attenuation. The correct interpretation of attenuation, however, is a long-standing problem. The usual approach to solution of this problem is to assume that the physical phenomena which produce attenuation make independent contributions to the measured result. One then characterizes the measured attenuation coefficient as a summation of coefficients resulting from (1) intrinsic attenuation (that resulting from viscous and thermal losses in the propagating medium as well as grain boundary scattering); (2) attenuation resulting from diffraction; and (3) attenuation resulting from a lack of parallelism between the ultrasonic source and the receiver. This thesis is an attempt not only to point out that (2) and (3) are not truly independent, but also to demonstrate how they can be interpreted simultaneously.

In his Theory of Sound first published in 1878, Lord Rayleigh (1950) gave the mathematical form of the diffraction integral. In 1886 Lommel published a solution of the same diffraction integral as applied to the propagation of light by utilizing the Kirchhoff approximation for Fresnel diffraction. The solution, given in the form of an infinite sum of Bessel functions, is awkward to use (Gray and

Matthews (1931)). Huntington et al. (1948) published the first diffraction correction for propagation of ultrasonic waves by making a numerical integration of the tabulated data of Lommel. Numerous authors subsequently have provided improvements of the numerical integration process, the latest having been published by Benson and Kiyohara (1974). Rogers and Van Buren (1974) obtained an analytical solution of Lommel's diffraction integral. Their solution is applicable to the transmission of sound between two discs of the same size which are parallel to each other. However, the analytical solution has limited utility in the present situation because it gives the result of integrating over a receiver area rather than the value of pressure at a single point in the diffraction field.

All the above models assume that the propagation medium is a lossless liquid. Papadakis (1975) studied the propagation of ultrasonic waves in a solid and states: "The solution for fluids applies adequately to isotropic solids as long as the transducer is bonded adequately to one of a pair of plane parallel faces of a slab considerably larger in lateral extent than the transducer diameter" (p. 154).

In all these studies the receiver and the source conveniently were assumed to be parallel. It has been known for some time that measurements of ultrasonic attenuation are seriously affected by nonparallelism of the source and the receiver. In their review article Breazeale et al. (1981) state "among the less easily evaluated errors are those arising from . . . phase cancellation resulting from lack of parallelism of the transducers, from material inhomogeneity, and from diffraction" (p. 68).

Truell and Oates (1963) studied the effect of nonparallelism of source and receiver. Their study showed that the diffraction pattern observed in a sample of wedge angle γ was modulated after n reflections by a function of the form $2J_1((2ka\ n\gamma)/2ka\ n\gamma)$. They then gave a mathematical treatment to explain this modulation phenomenon on the basis of phase cancellation of infinite plane waves. Truell et al. (1969) suggested that the form of the function could be used as a means of predicting the degree of parallelism required for a given value of ka to avoid the modulation effect. They also showed that the model's ability to predict the shape of the modulation was much better at high frequency (85 MHz) than at low frequency (35 MHz). Calder (1978) introduced a modification to the Truell and Oates model by correcting for the inhomogeneity of the sample. He applied his correction to a wedged sample and to a hemispherical reflector. In his case the Truell and Oates model significantly corrected for the modulation in the case of the hemispherical reflection; however, it was not able to correct for the modulation observed with the wedged sample.

In this thesis the Truell and Oates model is shown to be inappropriate for the frequency range 3 to 9 MHz in wedged steel samples. Next, the Truell and Oates model is modified by the removal of the plane wave approximation. This procedure makes it necessary to define the pressure at a point in the diffraction field. Then, the point values of the pressure are numerically integrated over the receiver area. Such an integration can be performed only after a definition of the relative position of the receiver and the displaced and rotated

wave field has been made. An inherent characteristic of this procedure is the lack of separability of the effects of diffraction and non-parallelism of the sample surfaces. The result is an improved model which is able to account for a number of experimental observations.

CHAPTER II

THEORETICAL ANALYSIS

A. WAVE PROPAGATION THEORY

1. Wave Attenuation

a. Definition of α, the attenuation parameter. If a pressure disturbance of the form $P(t) = P_0 e^{j\omega t}$ propagates a distance Δx from a point x_0 to a point x, then the pressure measured at the point x will be of the form:

$$P(x,t) = P_0 e^{j(\omega t - k\Delta x)} \quad . \tag{2-1}$$

An expression for an attenuated wave is obtained by assuming that the wave vector k is complex and given by:

$$k = k_0 - j\alpha \tag{2-2}$$

where α is the attenuation coefficient which is assumed to be constant. Equation (2-1) then becomes

$$P(x,t) = [e^{-\alpha\Delta x}]\ P_0 e^{j(\omega t - k_0\Delta x)} \quad . \tag{2-3}$$

The bracketed term expresses the manner in which the attenuation coefficient α affects the amplitude values. If we now take the modulus of Eq. (2-3), we obtain

$$P_{max}(x) = P_0 e^{-\alpha \Delta x} \quad . \tag{2-4}$$

From Eq. (2-4), then, α can be expressed as

$$\alpha = - \frac{1}{\Delta x} \ln \left[\frac{P_{max}(x)}{P_0} \right] \tag{2-5}$$

or equivalently as

$$\alpha = \frac{20}{\Delta x} \log_{10} \left[\frac{P_0}{P_{max}(x)} \right] \quad . \tag{2-6}$$

The unit of α in this case is db per unit of length of Δx.

b. The attenuation correction. If one wants to correct for attenuation, he must first examine the physical causes of this phenomenon. In general, the causes of attenuation are divided into two categories: the intrinsic attenuation phenomena α_i and the geometric attenuation phenomena α_g. These two categories are assumed to be independent of each other such that we can express α as:

$$\alpha = \alpha_i + \alpha_g \quad . \tag{2-7}$$

The intrinsic attenuation α_i is a measure of the loss of energy of the pressure wave. In a solid which is reacting as a continuum most of the intrinsic attenuation measured comes from the phase delay between the density function and the pressure function. Therefore, in a given homogeneous isotropic medium the total intrinsic attenuation α_i

experienced by a wave propagating at a frequency f_0 can be expressed, at least in the linear approximation, as a constant α_i. Then to obtain a value of intrinsic attenuation one can first correct a measured pressure value for geometrical attenuation and use this corrected pressure in Eq. (2-6).

The geometrical attenuation phenomenon is the one that will be studied in greater detail as it is significantly affected by many geometrical factors such as parallelism of the faces of the solid and diffraction which have been adjusted during the course of this investigation.

2. The Diffraction Theory

a. The diffraction model. We will assume that a source of pressure disturbance behaves as a circular piston in an infinite rigid baffle. Then the magnitude of the disturbance at any point on the source can be described either in terms of maximum pressure P_0 or maximum velocity U_0 as:

$$P(t) = P_0 e^{j\omega t} \tag{2-8}$$

$$U(t) = jU_0 e^{j\omega t} \tag{2-9}$$

where ω is the angular frequency of the disturbance. If this disturbance is now allowed to propagate into a lossless homogeneous isotropic fluid, its radiation pattern can be described by the use of classical wave theory. Using Huygens' principle we then approximate the piston by subdividing the area into small point sources and use the

additivity theorem to obtain the resulting effect of all these small sources at a field point.

Kinsler et al. (1982) give the radiation pattern of a small source (of any shape)[1] which is located in an infinite baffle as:

$$dP(R,t) = \frac{1}{R_0}\left[\frac{\rho_0 C U_0 k}{2\pi} dS' [j\, e^{j(\omega t - kR)}]\right] \qquad (2\text{-}10)$$

where

R is the distance from the center of the source to the field point;

ρ_0 is the medium density;

C is the velocity of propagation of the pulsation through the medium;

U_0 is the maximum velocity of the surface;

k is the wave vector;

dP is the pressure value; and

dS′ is the pulsating surface.

The pressure at a field point, defined by the spherical coordinate (R_0,θ) shown in Figure II-1, is given by the integration of Eq. (2-10) over S′, the source surface. One then obtains the diffraction integral:

$$P(R_0,\theta,t) = \frac{j\,\rho_0\,CU_0}{2\pi}\int_{S'} \frac{e^{j(\omega t - kR)}}{R}\, dS' \,. \qquad (2\text{-}11)$$

---

[1] Appendix A shows why for small sources the shape does not make any difference to the radiation pattern.

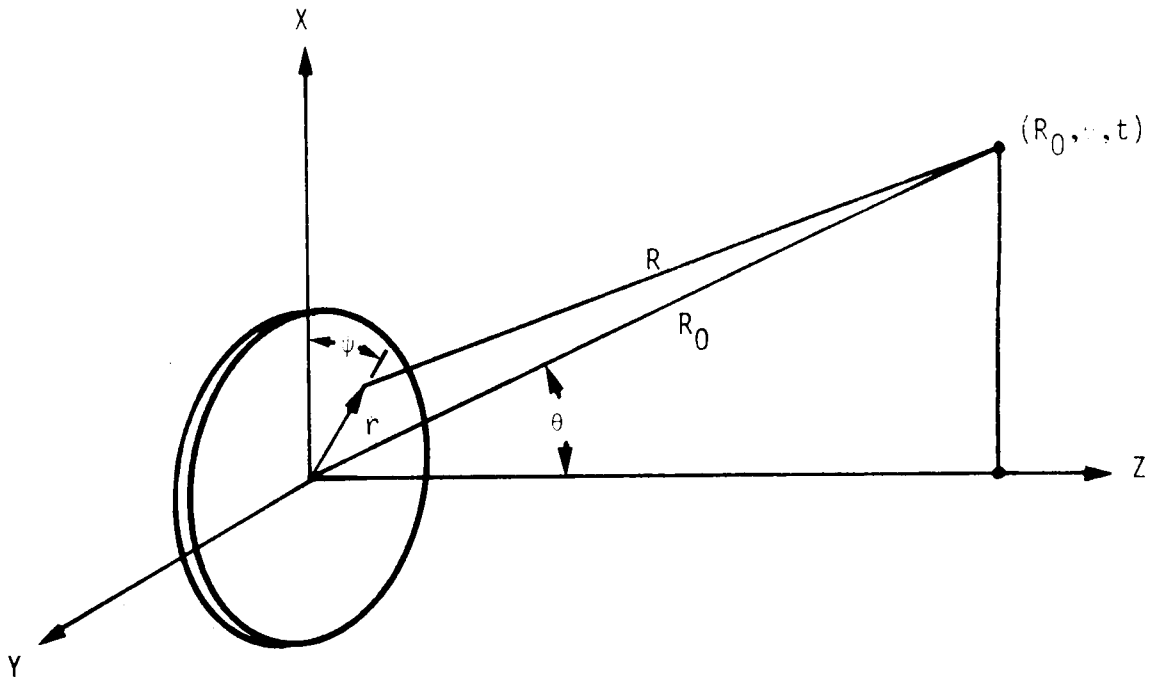


Figure II-1. Geometry Used in Deriving the Radiation Characteristics of a Piston Source.

This integral also is referred to as Rayleigh's integral and it does not have a closed form solution. However, a number of numerical integrations of this integral have been made and the result of one of them is shown in Figure II-2.

b. The pressure on the axis. The pressure in the field along the Z axis is one of the few quantities which can be analytically obtained from the piston model without further approximation. From Eq. (2-11):

$$P(z,0,t) = \frac{j\,\rho_0\,CU_0k}{2\pi}\,e^{j(\omega t)}\int_0^a \frac{e^{-jk(r^2+z^2)^{1/2}}}{(r^2+z^2)^{1/2}}\,2\pi r dr \qquad (2\text{-}12)$$

since:

$$\frac{r}{(z^2+r^2)}\,e^{-jk(z^2+r^2)^{1/2}} = -\frac{d}{dr}\,\frac{e^{-jk(z^2+r^2)}}{jk}\,. \qquad (2\text{-}13)$$

Then we obtain

$$P(z,0,t) = \rho_0\,CU_0\,e^{j\omega t}[e^{-jkz} - e^{-jk(z^2+a^2)^{1/2}}]\,. \qquad (2\text{-}14)$$

The magnitude of this expression is the pressure on the axis P_{axis}:

$$P_{axis} = 2\rho_0\,CU_0\left|\sin\{\tfrac{1}{2}\,kz[(1+(a/z)^2)^{1/2} - 1]\}\right|\,. \qquad (2\text{-}15)$$

When the value of z/a is much larger than ka, then P_{axis} simplifies to an asymptotic expression P_{sph} which is the spherically diverging wave expected at large distances:

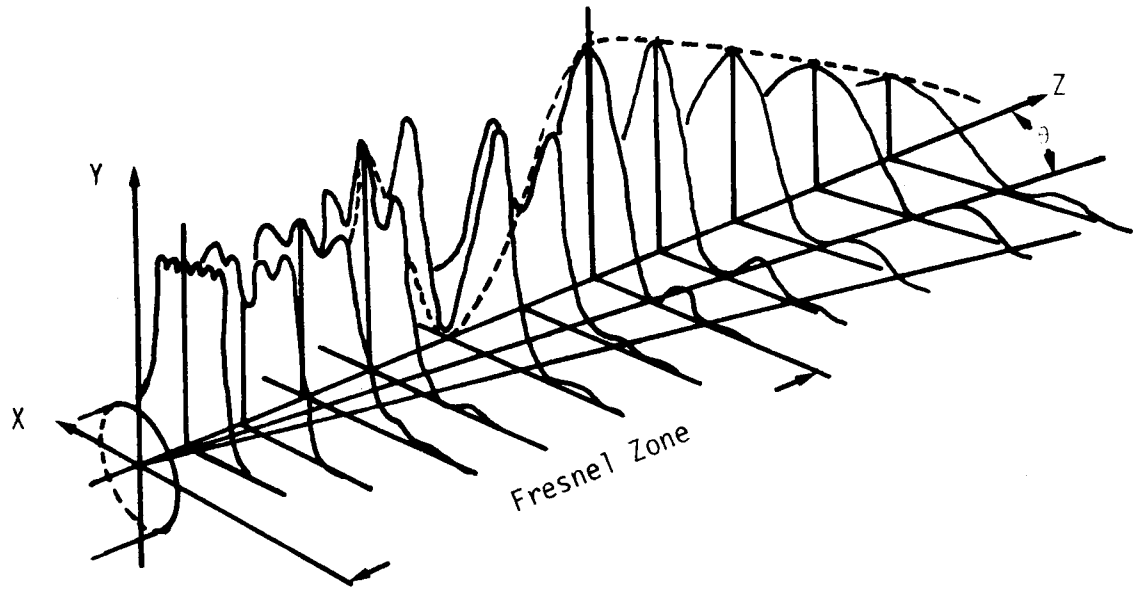


Figure II-2. The Shape of the Normalized Values of Pressure in a Plane Normal to the Direction of Propagation (from Mercier (1976)).

$$P_{sph} = \frac{\rho_0}{2z} CU_0 \, ka^2 \tag{2-16}$$

$$P_{sph}(z,t) = \frac{\rho_0}{2z} CU_0 \, ka^2 \, e^{j(\omega t - kz)} \, . \tag{2-17}$$

A comparison of the values of P obtained for Eqs. (2-15) and (2-17), shown in Figure II-3, shows that P_{sph} does not converge to within 10% of P_{axis} until a distance of twice the farfield distance z_f is achieved. The parameter z_f is defined as the axial distance to the last maximum of the axial pressure and is given by Krautkramer (1977) as:

$$z_f = (4a^2 + \lambda^2)/4\lambda \tag{2-18}$$

where a is the radius of the source element and λ is the wavelength of the wave.

c. The pressure in the farfield. An analytical form of the diffraction integral can be obtained by noting that for $R_0 >> a$ the value of R is adequately approximated by: (1) R_0 in the denominator and (2) by $R_0 - r \sin\theta\cos\psi$ in the more sensitive phase term. Then Eq. (2-11) can be integrated to give:

$$P(R_0,\theta,t) = \frac{\rho_0 \, CU_0}{2R_0} ka^2 \, e^{j(\omega t - kR_0)} \left[\frac{2J_1(ka \sin\theta)}{ka \sin\theta}\right] \, . \tag{2-19}$$

Then from Eq. (2-16)

$$P(R_0,\theta,t) = P_{sph}(R_0)\left[\frac{2J_1(ka \sin\theta)}{ka \sin\theta}\right] e^{j(\omega t - kR_0)} \tag{2-20}$$

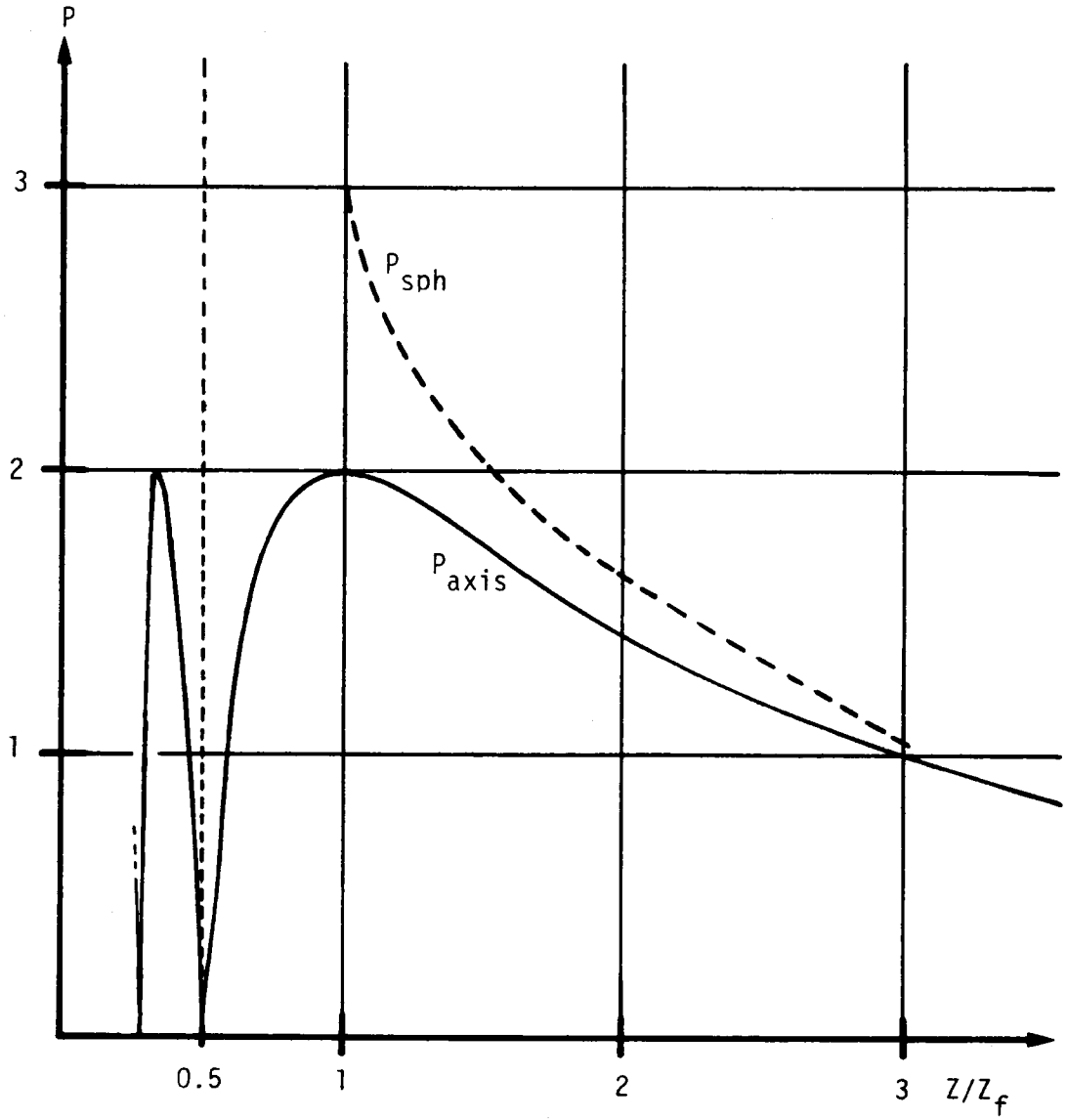


Figure II-3. Comparison of Pressure on Axis for P_0 = 1 (from Krautkramer (1977)).

where the spherical dependence $P_{sph}(R_0,t)$ is expressed by Eq. (2-11) when Z, the axial distance, is equal to R_0. The remaining term includes all the angle dependence and is commonly referred to as the directivity function. A plot of $[2J_1(ka\ \sin\theta)/(ka\ \sin\theta)]$ is shown in Figure II-4. It is important to note that in the farfield the angle θ gives the approximate direction of propagation of the wave on the wavefront, i.e., along the radius R_0 and that the function $H(\theta_i)$ becomes much more sensitive to variations of θ_i as the value of the parameter ka is increased. The polar diagram obtained from Krautkramer (1977) and included in Figure II-5 clearly shows this relationship.

d. Average pressure on the receiver. In a pulse echo system one can obtain the average pressure on the receiver by integrating Eq. (2-11) over the receiver area. Rogers and Van Buren (1974) have solved analytically this problem using the Fresnel[1] diffraction approximation and obtained a diffraction correction parameter D given by:

$$D = 1 - e^{-j(2\pi/S)}[J_0(2\pi/S) + j\ J_1(2\pi/S)] \qquad (2\text{-}21)$$

where $S = 2\pi Z/ka^2$ is the normalized propagation distance.

---

[1] In the Fresnel approximation one replaces R in Eq. (2-11) by Z in the denominator and by $Z + (r^2 + r'^2 - 2rr'\cos\psi')/2Z$ where the prime coordinates are the source coordinates. (See Gray and Mathews (1931).)

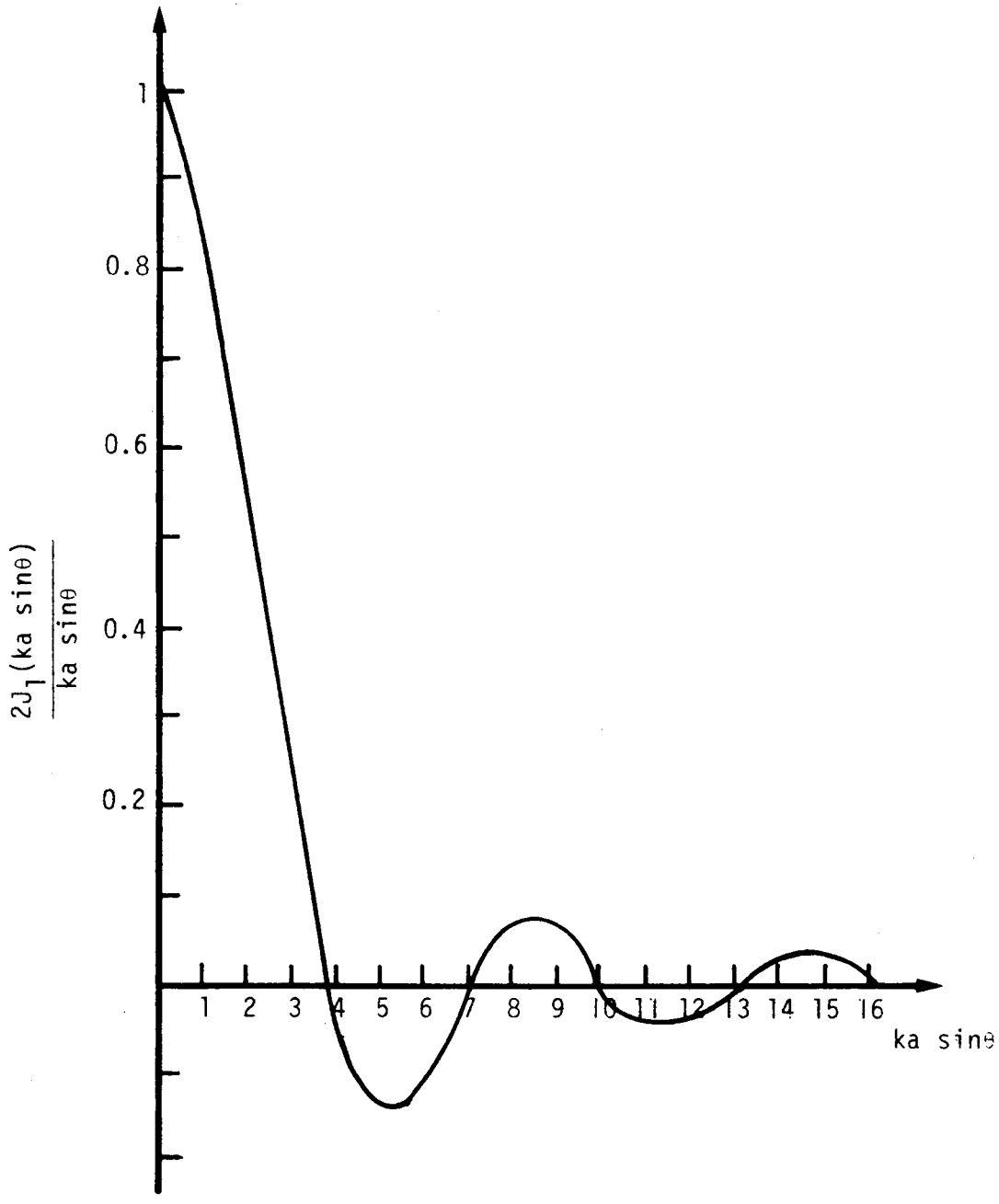
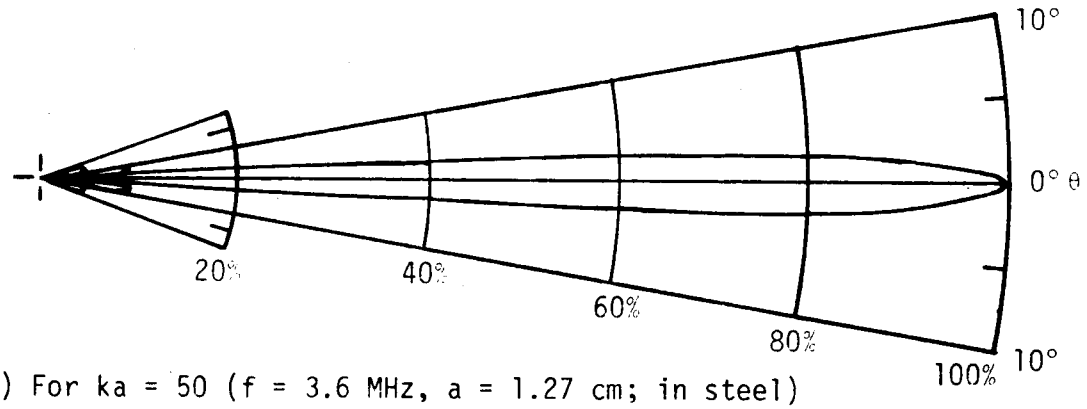
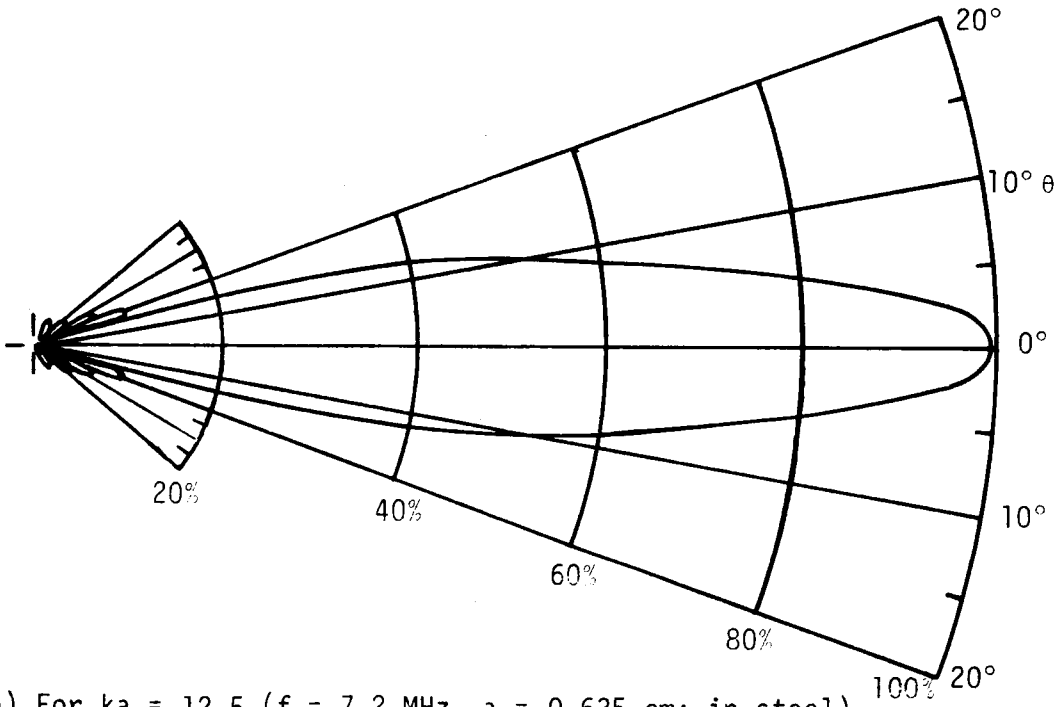


Figure II-4. Functional Behavior of $2J_1(ka \sin\theta)/ka \sin\theta$ (from Kinsler et al. (1982)).



(a) For ka = 50 (f = 3.6 MHz, a = 1.27 cm; in steel)



(b) For ka = 12.5 (f = 7.2 MHz, a = 0.635 cm; in steel)

Figure II-5. Directional Characteristic H(θ) (from Krautkramer (1977)).

B. GEOMETRICAL CORRECTION MODELS

1. The Plane Wave Correction Model

As will be shown in the results, significant deviations from the diffraction model are observed in the echo train of a wedged sample. Truell and Oates (1963) suggested a model to explain the deviation from the diffraction pattern based on the geometry of wedged samples. This model will be described here.

a. The geometry of propagation in a wedged sample. Let us assume that a sinusoidal disturbance of frequency f_0 originating at a time t_0 and having radial symmetry about an origin O, begins propagating along the normal to the upper surface of a wedge of angle γ as shown in Figure II-6. At any time $t > t_0$ the center of symmetry of this disturbance is located along the axis of propagation of this wave; i.e., at the center of the wavefront. Now, consider the displacement of the center of the wavefront of the disturbance as the wave is multiply reflected within the sample. This displacement occurs along a path described by a ray folded by reflection between the faces of the wedge. At every reflection from the lower face the relative angle γ_n between the upper surface and the normal to the propagation direction of the wave is increased by 2γ. After n reflections from the lower surface, the relative angle γ_n is given by:

$$\gamma_n = 2n\gamma. \tag{2-22}$$

Furthermore, it is evident that as the wave propagates its symmetry axis Z will wander away from the receiver origin O.

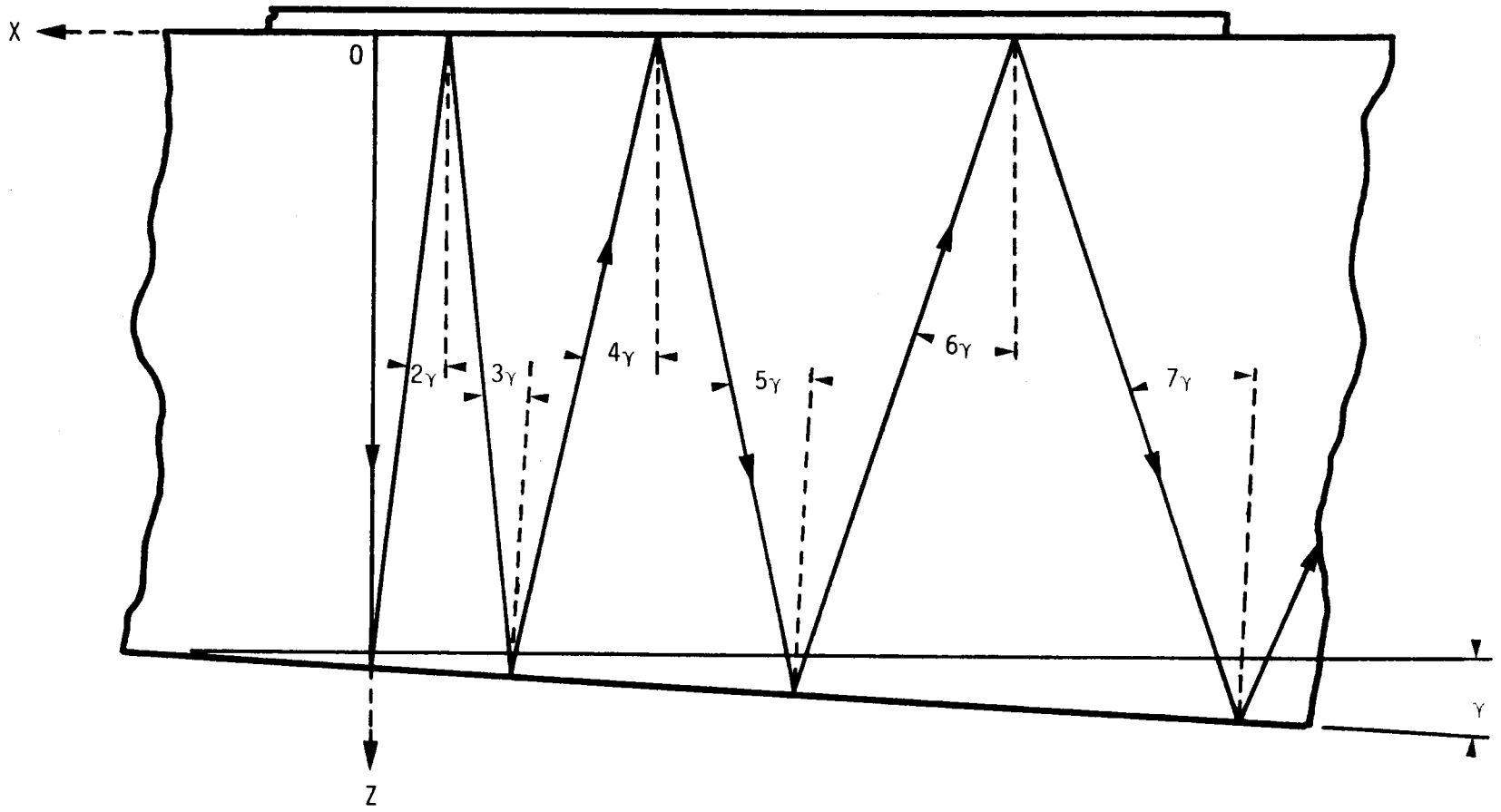


Figure II-6. Propagation Path of the Center of the Disturbance.

b. The theory of Truell and Oates. Truell and Oates (1963) gave a theoretical model to explain the rapid fluctuation of amplitude observed in the echo train of a circular piezoelectric receiver when a wedged sample is used. They assumed that the wavefront was effectively plane and that the fluctuations in pulse height could be accounted for by the variations in the receiver signal that resulted from phase cancellation of the wavefronts across the receiving transducer. Assuming the effective translation of the receiver is negligible, then the pressure function at a point (R_0,θ,t) after n reflections from the lower surface of the wedge can be expressed as:

$$P(R_0,\theta,t)_n = e^{j\{\omega t-k[2nL-x\sin\gamma_n]} \quad . \tag{2-23}$$

This expression must be integrated over the circular receiver to obtain the average pressure $(\tilde{P})_n$:

$$(\tilde{P})_n = \frac{e^{j\omega t}}{\pi a^2} \int_{-a}^{a} 2(a^2 - x^2)^{1/2} \, e^{-jk(2nL-x\sin\gamma_n)} dx \quad . \tag{2-24}$$

The result of this integration gives:

$$(\tilde{P})_n = \sin(\omega t - 2knL)\, H(\gamma_n) \tag{2-25}$$

where

$$H(\gamma_n) = \frac{2J_1[ka \sin\gamma_n]}{ka \sin\gamma_n} . \qquad (2\text{-}26)$$

The form of this function is given by the magnitude of the directivity function defined in Eq. (2-20).

c. The average pressure on the receiver. In the Truell and Oates model, the function obtained in Eq. (2-25) is assumed to modulate the exponential diffraction pattern such that both effects can be corrected for separately. The expression of the average amplitude on the receiver is then given by the multiplication of the diffraction correction parameter D given by Eq. (2-22) and $H(\gamma_n)$. Therefore, the magnitude of the average pressure $\tilde{P}$ is given by:

$$|\tilde{P}| = DH(\gamma_n) . \qquad (2\text{-}27)$$

The range of $|\tilde{P}|$ may go from 0 to 1 and conversely the geometrical attenuation according to the plane wave model goes from $-\infty$ to 0.

2. The Diffracted Wave Model

As will be seen in the Results section, the plane wave model which assumes independence of the diffraction and wedge geometry correction does not satisfactorily describe the echo train observed. A new approach combining both the diffraction theory and the description of the phase cancellation will be developed for the wedge sample geometry.

a. Model of the physical situation. If one examines the diffraction model given in Eq. (2-11) and depicted by Figure II-2 (p. 11), one realizes that assuming a plane wave with a constant pressure distribution is a very crude approximation of the physical situation. Furthermore, this description is made in relation to a fixed propagation axis. However, as is obvious from Figure II-6, the propagation axis is rotated and translated in relation to the source/receiver element as the wave is multiply reflected in the sample. An example of an analogous situation for a unidirectional propagation path is shown schematically in Figure II-7. Using this physical model we will define the average pressure resulting on the receiver when the propagation distance is larger than the nearfield distance. First, a modification of the farfield approximation will be done to improve its convergence. Second, a coordinate transformation system will be defined such that the unidirectional diffraction theory can be applied to the propagation in a wedge sample. Third, an average pressure will be obtained by numerical integration of the pressure function over the receiver area.

b. Modification of the solution of the diffraction integral in the farfield. A study of the convergence of the farfield approximation, given in Eq. (2-20), to a numerical approximation of the diffraction integral was made by Rose (1975). He concluded that the directivity function $(2J_1(u)/u)$ seemed to converge much more rapidly to the shape of the numerical values than the value of P_{sph} to the value of pressure on axis P_{axis}. In order to obtain a more rapid convergence of the

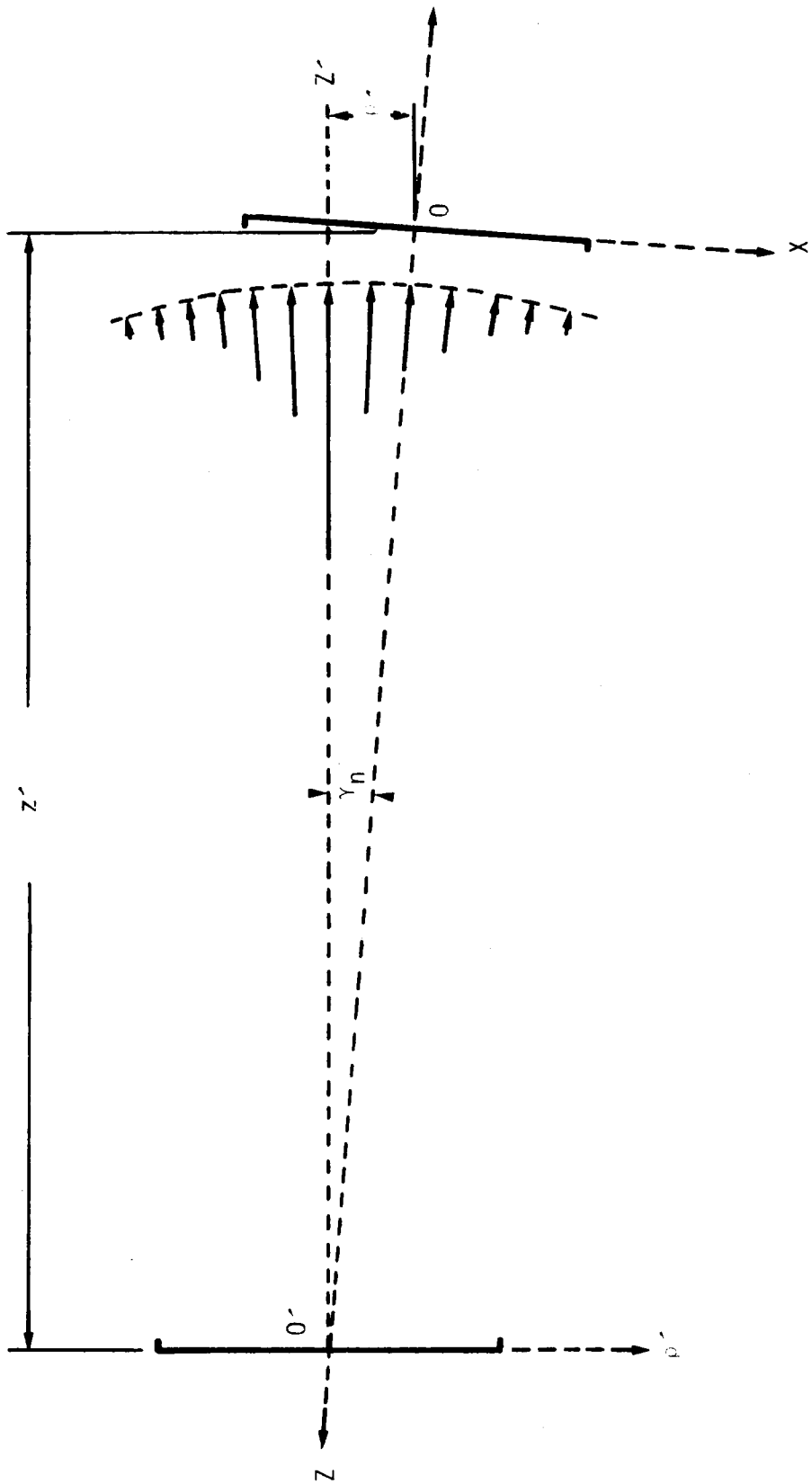


Figure II-7. Schematic Representation of the Wavefront Showing the Amplitude Distribution and the Relative Source and Receiver Position after n Reflections.

solution, the value of P_{sph} in Eq. (2-20) is replaced by the value of P_{axis} from Eq. (2-15). The new equation for the pressure is then:

$$P(R_0,\theta,t) = P_{axis}(R_0)[2J_1(ka\sin\theta)/(ka\sin\theta)]e^{j(\omega t-kR_0)} . \quad (2\text{-}28)$$

A numerical integration of this integral was done over a receiver of 1.27 cm radius using the IMSL function DBLINT which is a cautious Romberg quadratic numerical integration process. This result is compared with the closed form analytical expression of the diffraction integral given by Eq. (2-22). Figure II-8 shows the value of Eq. (2-28) as a means of improving the convergence of the expression of the pressure in the farfield.

The normalized plot of average pressure shown in Figure II-8 is then used to extend the validity of the numerical integration of Eq. (2-28) to points having a propagation distance smaller than three times Z_f. A correction is then applied to all the average pressure $\tilde{P}$ subsequently obtained by integrating this equation over the receiver surface. The correction is applied by multiplying the average pressure by the ratio of the average pressure obtained from Rogers and Van Buren's solution to the average pressure obtained by integrating Eq. (2-28) for a piezoelectric element of 1.27 cm radius at 4 MHz. This radio was verified to be the same to within less than 1% whether the radius is 0.635 cm or 1.27 cm or the frequency 2, 4, 6, or 8 MHz.

c. The coordinate transformations.

The new coordinate system. To define a new coordinate system it will be necessary to define an imaginary source of origin O_n' located

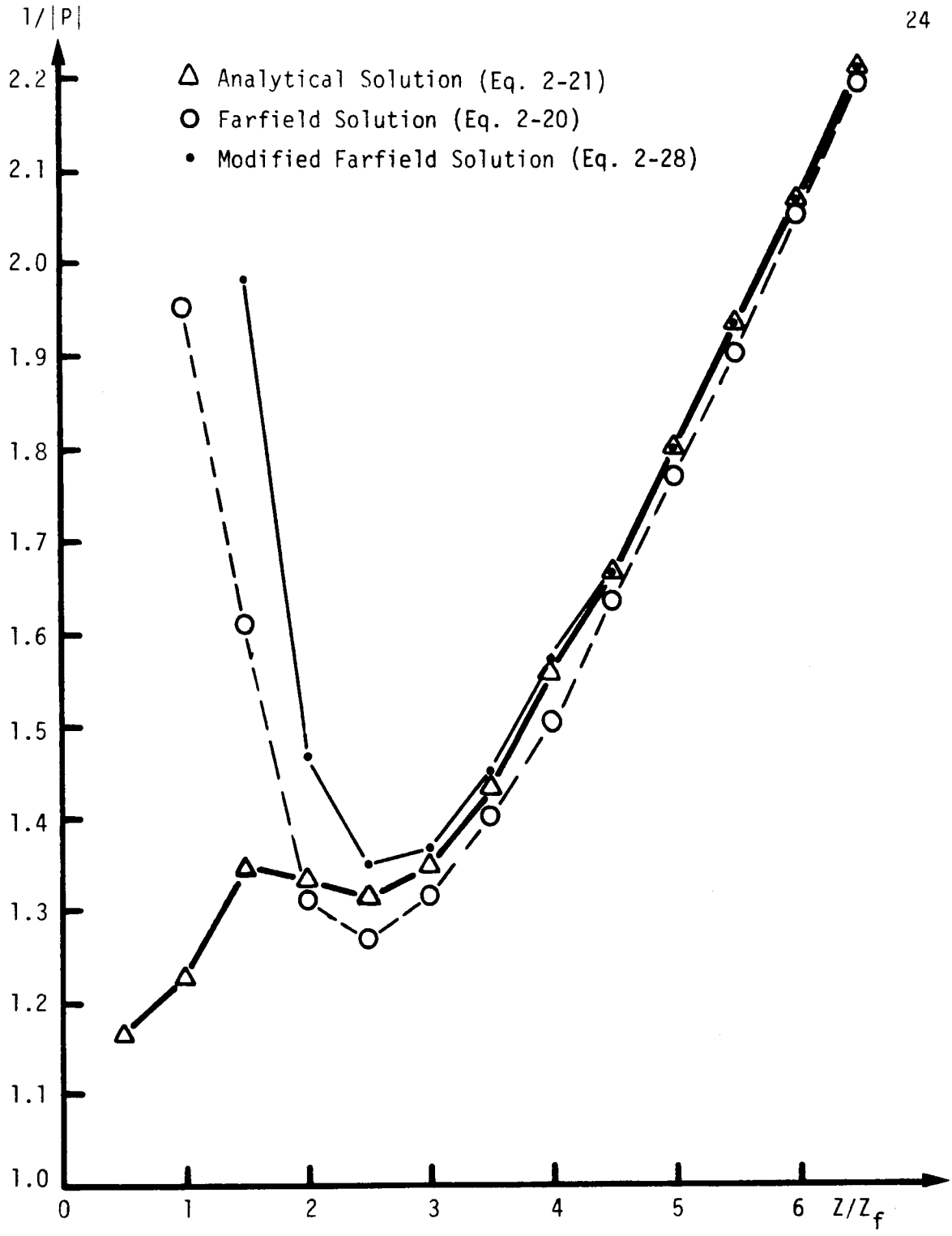


Figure II-8. Inverse of the Average Pressure on the Receiver as a Function of Normalized Propagation Distance.

along the axis of symmetry Z'_n of the wave such that an equivalent unidirectional path can be associated with the wave. In this system the axis Z'_n is defined to be coincident with the axis of symmetry and the direction of propagation of the wave after n reflections from the lower face. From symmetry consideration it will then be mathematically simpler to use a cylindrical coordinate system described by the three orthogonal axes ρ'_n, ϕ'_n, and Z'_n.

Position of the imaginary source origin O'_n. The radial coordinate $[\rho'(0,0)]_n$ of the center O of the receiving element is obtained by considering the right triangle, formed by the intercept of the Z axis, the Z'_n axis and the distance $[\rho'(0,0)]_n$, in Figure II-9. The angle between the normal to the surface and the axis Z'_n is defined by Eq. (2-22) as γ_n. Its opposite angle, defined by the axes Z and Z'_n, must also be γ_n since Z is normal to the surface. Then we have

$$[\rho'(0,0)]_n = n\ L\ \sin\gamma_n\ , \tag{2-29}$$

where L is the sample length measured at the center of the receiver. The angle, defined by the distance $[\rho'(0,0)]_n$, and the surface must be equal to γ_n since its two sides are respectively perpendicular to the normal to the surface and to the Z'_n axis. Then its bisectrix will cut the Z'_n axis at a point $[Z'_{par}]_n$. Consider now the triangle formed by the bisectrix, the Z and the Z'_n axis. In this triangle the angle $\hat{A}$ opposite to the Z'_n axis side is given by

$$\hat{A} = \pi/2 - \gamma_n/2\ . \tag{2-30}$$

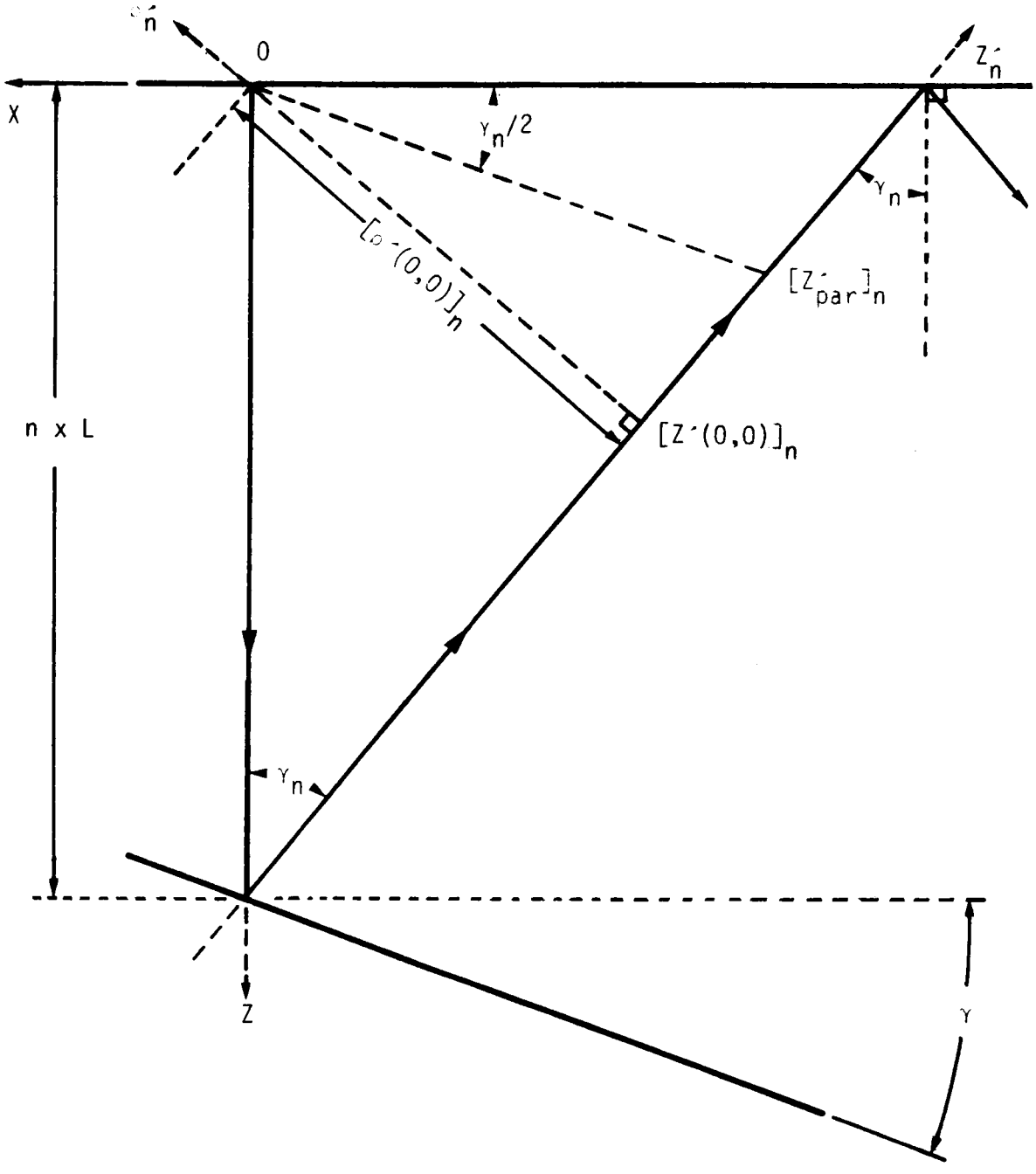


Figure II-9. Geometrical Relationship Existing for n = 1.

Since the angle $\hat{B}$ opposed to the bisectrix has been defined previously as γ_n, then the angle $\hat{C}$ opposite to the Z axis is given by:

$$\hat{C} = \pi - \hat{B} - \hat{A} \tag{2-31}$$

or

$$\hat{C} = \pi - \gamma_n - (\pi/2 - \gamma_n/2) = \pi/2 - \gamma_n/2 \ . \tag{2-32}$$

Since $\hat{C}$ equals $\hat{A}$, then their sides are equal and since the Z axis side is equal to n x L, then the Z'_n axis side is also equal to n x L. This means that the propagation path of the wave from 0 to $[Z'_{par}]_n$ is given by:

$$[Z'_{par}]_n = n \times L + n \times L = 2\ n\ L \ . \tag{2-33}$$

The magnitude of $[Z'_{par}]_n$ is the propagation distance of a wave between parallel faces after n reflections from the lower surface.

Now let us consider the right triangle formed by the distance $[\rho'(0,0)]_n$, the bisectrix and the Z'_n axis. The Z'_n axis side which we will call $\Delta Z'$, is given by:

$$\Delta Z' = [\rho'(0,0)]_n \tan(\gamma_n/2) \ . \tag{2-34}$$

The propagation path from 0 to $[Z(0,0)]_n$ is given by:

$$[Z'(0,0)]_n = [Z'_{par}]_n - \Delta Z' \ . \tag{2-35}$$

Then by combining (2-33), (2-34), and (2-35), we obtain the $[Z'(0,0)]_n$ coordinate as:

$$[Z'(0,0)]_n = n \times L\,[2 - \sin(\gamma_n)\,\tan(\gamma_n/2)]\ . \qquad (2\text{-}36)$$

The relative positions of the imaginary source origin O'_n and the receiver origin O are now defined by Eqs. (2-29) and (2-36). This geometrical relationship which has been shown to be exact for the first reflection is assumed to be exact for n reflections. It has been verified graphically to be exact for at least four reflections for different angles γ ranging from 1° to 5°. An example of such graphical construction is shown in Figure II-10.

Cylindrical coordinate of a point on the receiver surface. Consider the projection of the upper surface in the ρ'_n Z'_n plane cut along the X axis as shown in Figure II-11. The X axis, the parallel to the ρ'_n axis passing by the poing (0,0) and the parallel to the Z'_n axis passing by the point (x,0) form a right triangle of respective side x, $x\cos\gamma_n$ and $x\sin\gamma_n$. Then the intercept on the Z'_n axis of the point (x,0) is given by

$$[Z'(x,0)]_n = [Z'(0,0)]_n - x\sin\gamma_n\ . \qquad (2\text{-}37)$$

The points (x,y) and (x,0) must have the same Z'_n value since y is antiparallel to ϕ'_n. Therefore, Eq. (2-37) can be rewritten as:

$$[Z'(x,y)]_n = [Z'(0,0)]_n - x\sin\gamma_n\ . \qquad (2\text{-}38)$$

The intercept of the point (x,0) on the ρ'_n axis is similarly given by:

$$[\rho'(x,0)] = [\rho'(0,0)]_n + x\cos\gamma_n\ .$$

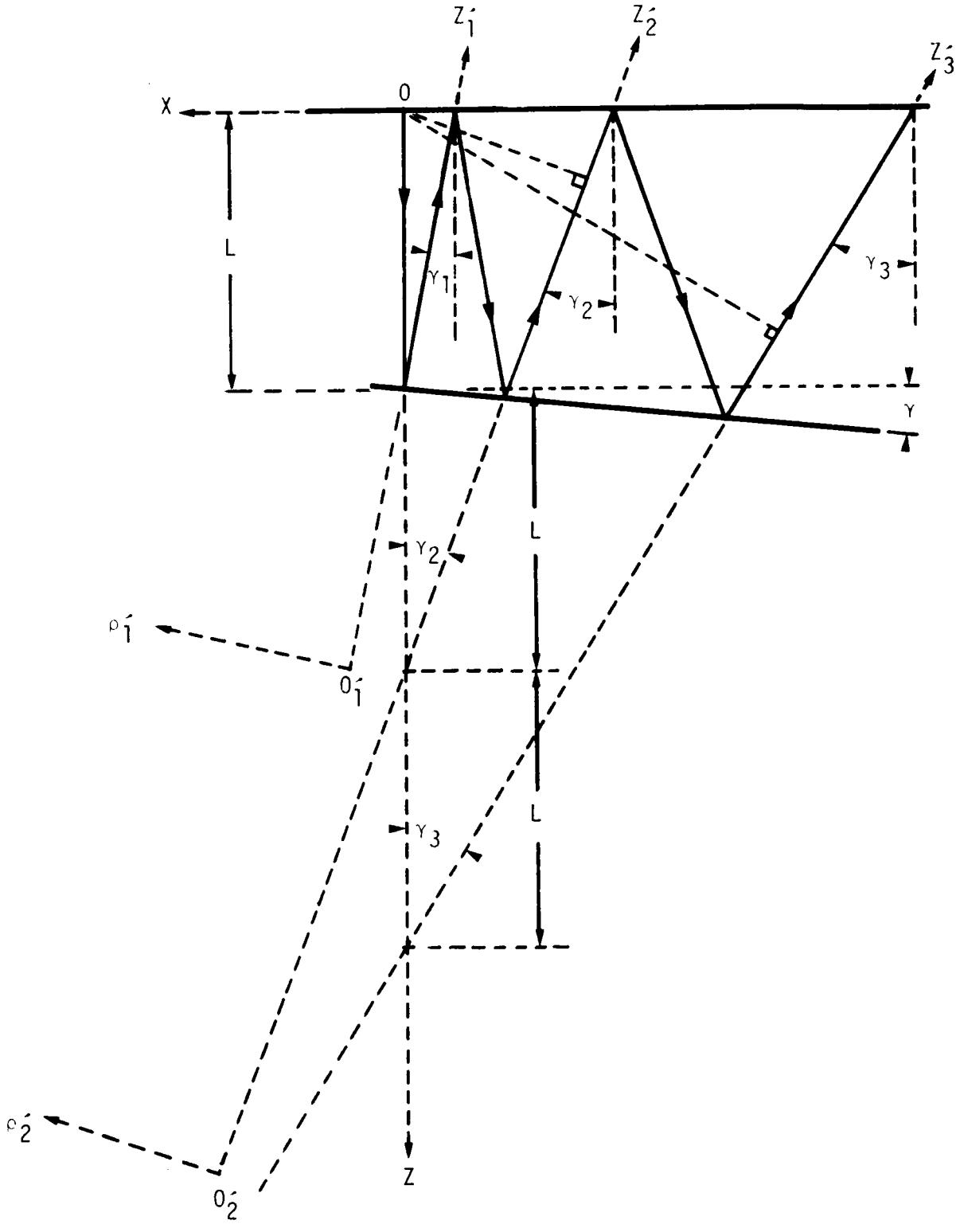


Figure II-10. Graphical Construction Showing the Geometrical Relations after Three Reflections.

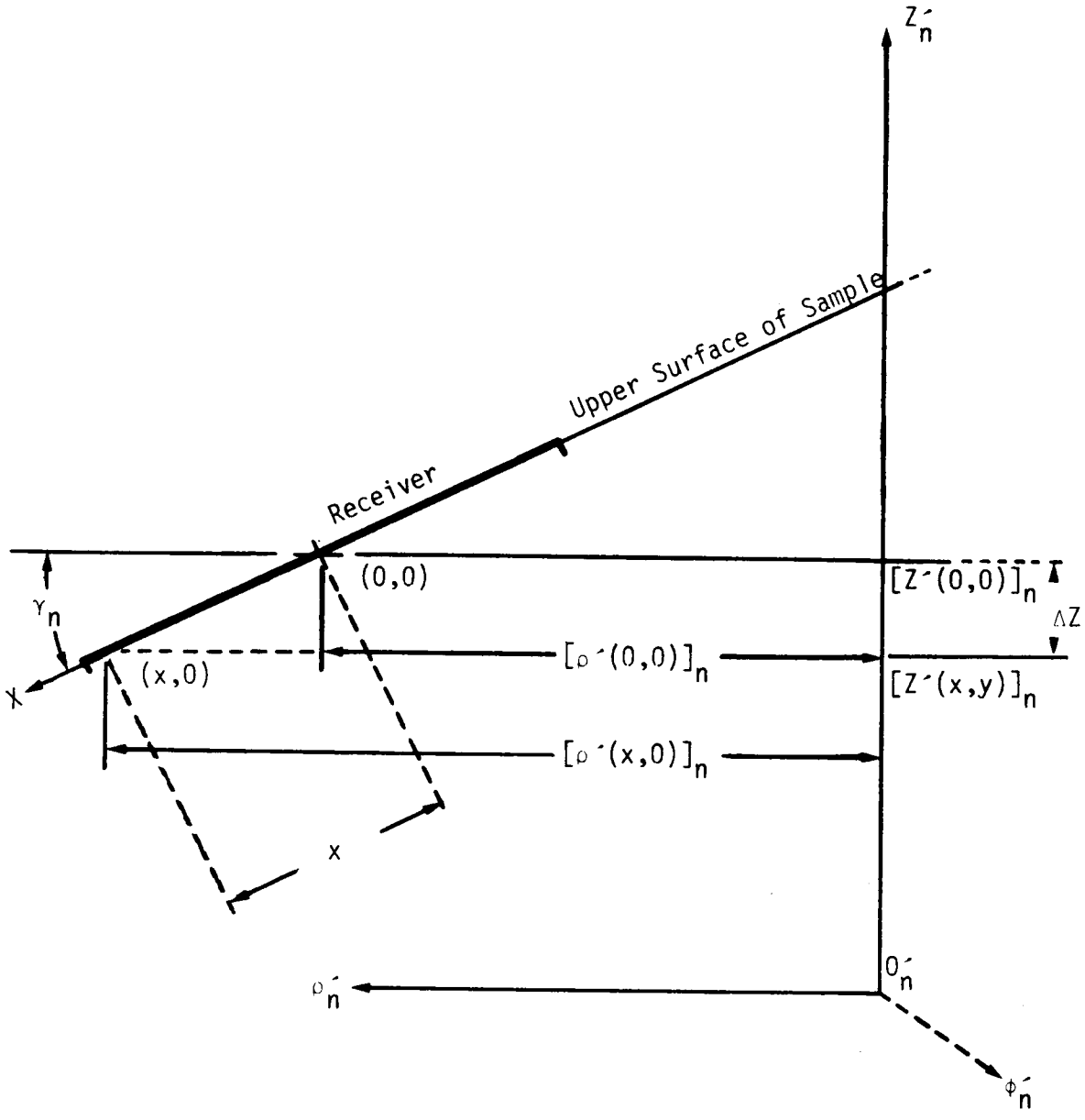


Figure II-11. Definition of the Receiver Coordinate (x,y) in the $\rho'_n Z'_n$ Plane.

Let us now consider the $\rho_n' \phi_n'$ plane cut along the parallel to the y axis formed by the point (x,0) and (x,y) as shown in Figure II-12. In the right triangle formed by the three points (x,0), (x,y), and $[0,Z'(x,y)]_n$, the distance between the last two points is $[\rho'(x,y)]_n$ and is given by:

$$[\rho'(x,y)]_n = [[\rho'(x,0)]^2 + y^2]^{1/2} \quad . \tag{2-39}$$

We can now convert x and y in terms of r and ψ by noting that

$$x = r \cos \psi \, , \tag{2-40}$$

$$y = r \sin \psi \, . \tag{2-41}$$

This means that we can define the diffraction field parameters R_0, θ in terms of r and ψ by using the following identities:

$$(R_0) = \{[\rho'(r,\psi)]^2 + [Z'(r,\psi)]_n^2\}^{1/2} \, , \tag{2-42}$$

$$(\theta)_n = \tan^{-1} \frac{[\rho'(r,\psi)]_n}{[Z'(r,\psi)]_n} \, . \tag{2.43}$$

d. The average pressure on the receiver. From the modified expression of the pressure P at a point in the field expressed by Eq. (2-28) and the relationship between R_0, θ and $(\rho',Z')_n$ defined by Eqs. (2-42) and (2-43), we can express the pressure at a point $(\rho',Z')_n$ as:

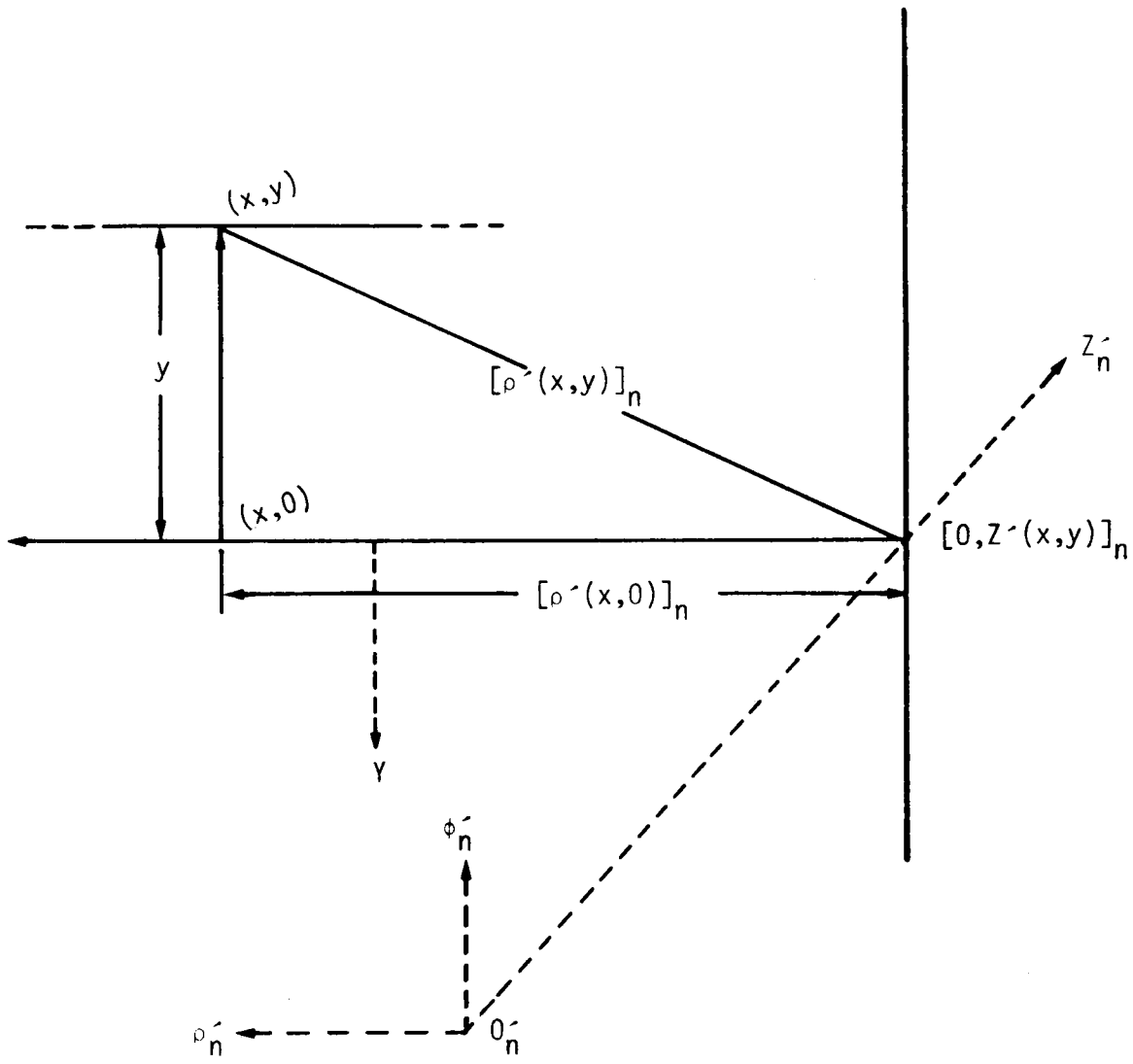


Figure II-12. Definition of the Coordinate $[\rho'(x,y)]_n$ in the $\rho'_n\phi'_n$ Plane.

$$P(\rho',z',t)_n = P_{axis}(R_0(\rho',z')_n)[2J_1(ka\sin\theta(\rho',z')_n)/ka\sin\theta(\rho',z')_n]$$
$$e^{j(\omega t - kR_0(\rho',z')_n)} . \qquad (2\text{-}44)$$

By using Eqs. (2-38)-(2-42) we obtain ρ' and z' as a function of r and ψ, the receiver coordinates. The average pressure $\tilde{P}_n(t)$ is obtained by integrating Eq. (2-44) over the circular receiver area of radius a. This gives:

$$\tilde{P}_n(t) = \frac{1}{\pi a^2}\int_{\psi=0}^{2\pi}\int_{r=0}^{a}|P[r,\psi]|_n e^{j[\omega t - kR_0(r,\psi)]} r\, dr\, d\psi . \qquad (2\text{-}45)$$

Since in the attenuation study we measure the maximum pressure, we need the magnitude of Eq. (2-45). Using the identity

$$e^{j\theta} = \cos\theta + j\sin\theta , \qquad (2\text{-}46)$$

Eq. (2-46) becomes

$$\tilde{P}_n(t) = \frac{1}{\pi a^2}\int_0^{2\pi}\int_0^{a}|P[r,\psi]|_n\{\cos[\omega t - kR_0(r,\psi)]$$
$$+ j\sin[\omega t - kR_0(r,\psi)]\}r\, dr\, d\psi . \qquad (2\text{-}47)$$

Since we need only the real part, then

$$\tilde{P}_n(t) = \frac{1}{\pi a^2}\int_0^{2\pi}\int_0^{a}|P[r,\psi]|_n\cos[\omega t - kR_0(r,\psi)]r\, dr\, d\psi . \qquad (2\text{-}48)$$

Since cos(A-B) is equal to cosA cosB + sinA sinB, then

$$\tilde{P}_n(t) = \frac{1}{\pi a^2}\{\cos\omega t \int_0^{2\pi}\int_0^a |P[r,\psi]|_n \cos kR_0(r,\psi) r\, dr\, d\psi$$

$$+ \sin\omega t \int_0^{2\pi}\int_0^a |P[r,\psi]|_n \sin kR_0(r,\psi) r\, dr\, d\psi\} \quad . \qquad (2\text{-}49)$$

These two integrals can now be evaluated numerically such that Eq. (2-49) becomes

$$\tilde{P}_n(t) = (\pi a^2)^{-1}\{\cos\omega t\, f_1 + \sin\omega t\, f_2\} \quad . \qquad (2\text{-}50)$$

The magnitude of $\tilde{P}_n(t)$ is given by

$$|\tilde{P}|_n = [\pi a^2]^{-1} \times [f_1^2 + f_2^2]^{1/2} \quad . \qquad (2\text{-}51)$$

According to the diffracted wave model, the parameter $|\tilde{P}|_n$ then represents the maximum average pressure impinging on a circular transmitter/receiver when a pressure wave subjected only to geometrical attenuation and of a magnitude of 1 is reflected n times from the lower face of a wedged sample. The range of $|\tilde{P}|_n$ goes from 1 to 0 and the corresponding range of α_g (the attenuation due to geometrical attenuation) goes from 0 to $-\infty$.

3. The Correction for Geometrical Attenuation

An amplitude correction factor $(CG)_n$ is defined as the ratio of the magnitude of the average pressure felt on a receiver of radius a when (1) an infinite plane wave is impinging normally on its surface

($\tilde{P} = 1$) to (2) the situation described by either Eq. (2-51) or (2-27).

$$(CG)_n = \frac{1}{|\tilde{P}|_n} . \tag{2-52}$$

Then after n reflections from the lower face of a wedge the magnitude of a measured average pressure $|P|_n$ can be corrected for geometrical effects to obtain a corrected average pressure $|P_c|_n$.

$$|P_c|_n = |P|_n \times |CG|_n . \tag{2-53}$$

Equivalently, $|P_c|_n$ is the magnitude of an infinite plane wave propagating normally to the receiver. The pressure P(t) in such a wave is given by:

$$P(t) = |P_c|_n \, e^{j(\omega t - kR_0(0,0)_n)} \tag{2-54}$$

where $R_0(0,0)_n$ is the distance from the center of the imaginary source $0_n'$ to the center of the receiver (0,0).

The geometrical attenuation correction process described in this section is coded in FORTRAN 10 language and included in Appendix B. The program calculates the attenuation between the first and the nth corrected echo of a given pulse echo setup specified by: (1) the velocity V of the ultrasonic wave in the sample, (2) the source radius a, (3) the frequency of the piezoelectric crystal f, (4) the non-parallelism angle γ, (5) the sample length L, and (6) the relative amplitude of the voltage from the piezoelectric crystal after n reflections A(n).

CHAPTER III

EXPERIMENTAL APPARATUS AND PROCEDURE

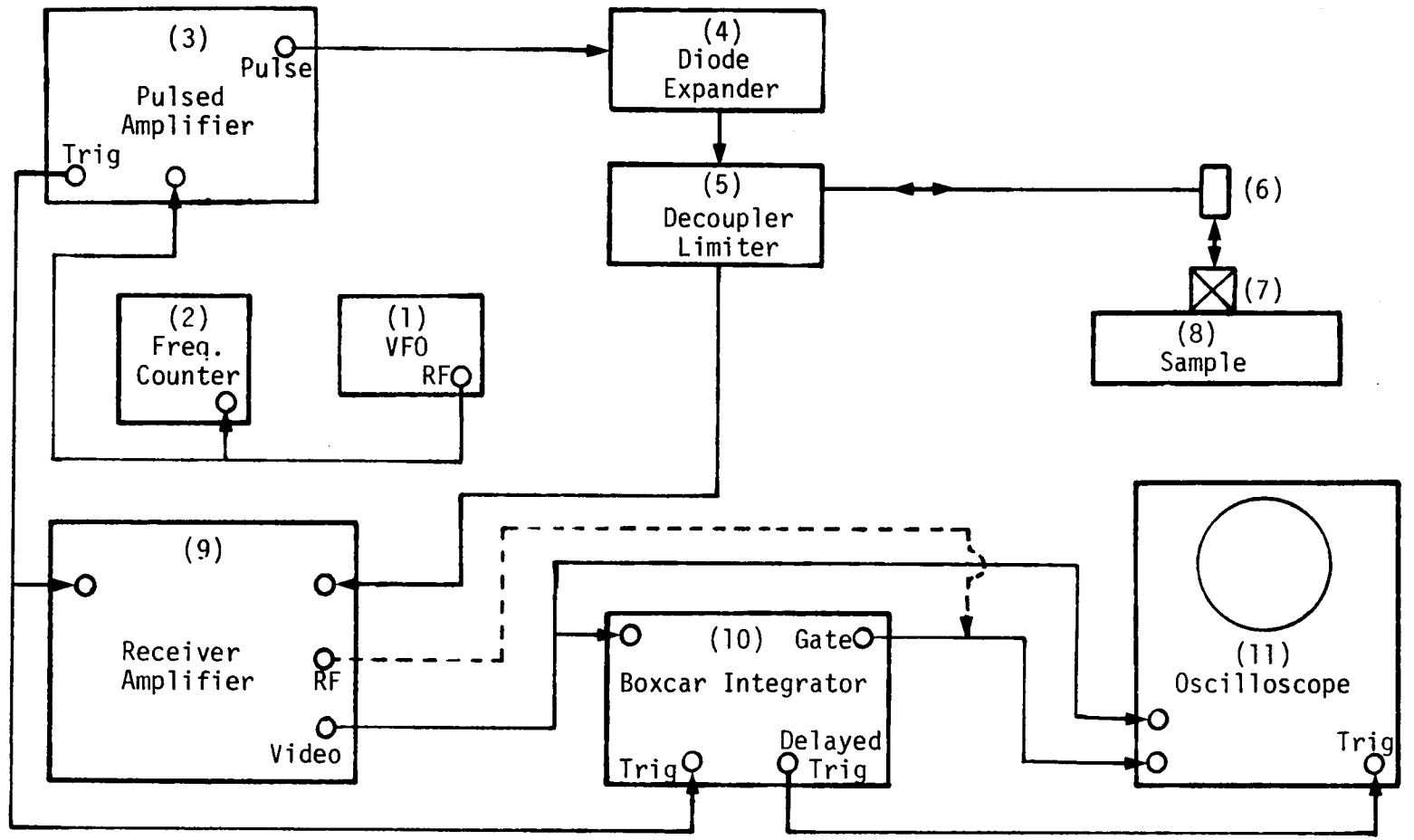
A. PURPOSE AND BACKGROUND

The purpose of this investigation is to gain insight into the propagation of ultrasonic waves in a wedged sample. Preparatory efforts were concentrated in three areas: sample definition and characterization; design of electronic setup for transmission and reception of electrical signal; design of a transducer for coupling of ultrasonic waves and electrical signal.

B. EXPERIMENTAL APPARATUS

1. Electronic Components

a. System description. The block diagram of the electronic system is shown in Figure III.1. A variable frequency oscillator (VFO) is used to generate an RF signal of a given frequency. This signal is then fed into a frequency counter and a gated pulsed amplifier. The pulsed amplifier sends out amplified pulses of this RF signal, at a specified pulse repetition frequency (PRF), to the diode expander. The diode expander eliminates undesirable low amplitude secondary pulses by the use of Zener diodes. The signal is then fed into a decoupler limiter. This decoupler sends the signal to the receiver and to the transducer and limits the amplitude of the signal fed to the receiver to avoid saturation of the receiver amplifier. The transducer



(1) General Radio Model 1211
(2) General Radio Type 1192-B
(3) Arenberg Model PG-650C
(4) Matec Diode Expander
(5) See Scott, 1975
(6) Tektronix 93Ω Terminator
(7) Transducer
(8) Steel Plate
(9) Matec Model 6600,
Plug In Type 750
(10) Princeton Appl. Res. Model 160
(11) HP Model 1740A (100 MHz)

Figure III.1. Electronic Circuits Used for Acoustical Measurements.

transforms these single frequency pulses into longitudinal pressure waves of ultrasonic frequency corresponding to the frequency sent by the VFO. As the wave propagates, an echo is eventually reflected back onto the transducer where the piezoelectric element transforms this pressure wave back into an electrical output having the frequency of the original signal, but of much lower amplitude. This echo is then retransmitted by the decoupler limiter to the receiver. The receiver contains a wide band (1 to 90 MHz) amplifier which can amplify received RF signals by up to 20 decibels. This signal is then rectified and can be amplified by up to 70 decibels by the second stage of this receiver. The rectified and amplified transducer response is then fed into the boxcar integrator and displayed on the oscilloscope. The position of that gate relative to the signal indicates the part of the signal that is averaged out and measured by the boxcar integrator. The synchronization of the pulser-receiver-boxcar integrator system is ensured by triggering all these elements from the pulser internal trigger. The oscilloscope is then triggered from the boxcar delayed trigger output.

b. System discussion. Pulse operation was selected over continuous wave for its superior immunity to cross-talk interference. Pulse-echo was selected over through transmission to minimize system alignment error. The need for accurate frequency measurements and short pulse length suggested the use of a VFO coupled to a gated amplifier rather than an integrated oscillator-pulser-receiver unit. As mentioned by Truell et al. (1969), this type of setup allows for excellent sensitivity to change in amplitudes for all values of

attenuation. A limiter is built into the receiver input; however, to avoid partial saturation of the receiver amplifier it is still necessary to use an external decoupler limiter. A diode expander is used to eliminate pulses of low level energy which appear immediately after the collapse of the main RF pulses[1] and last long enough to affect the first two returning echoes. Terminators of 93Ω impedance are used to provide impedance matching between the pulser and the transducer.

2. Transducer

a. Structure. A quartz, x-cut, crystal is used as a piezoelectric element for the generation and reception of the ultrasonic wave. As discussed in Krautkramer (1969), one of the chief advantages of quartz crystal over ceramic crystals such as barium titanate or lithium niobate is its mechanical strength which was necessary to allow for pressure application of the crystal on the sample. This pressure is applied by the use of a vise pressing on both the sample lower face and the transducer brass housing at the same time, as can be seen in Figure III.2. A photograph of the transducer parts is also shown in Figure III.3. The transducer parts were originally designed to be used with different types of immersion transducers [see Scott (1975)]. The main brass housing is maintained by the vise on a lucite crystal housing. This crystal housing is of the form of a ring with the upper side flat against the brass housing and a depression on the lower side. This

[1]This effect is generally caused by accumulation of low level piezoelectric energy in the ceramic capacitor of the oscillator circuit, which is coupled to the load after the collapse of the RF pulse.

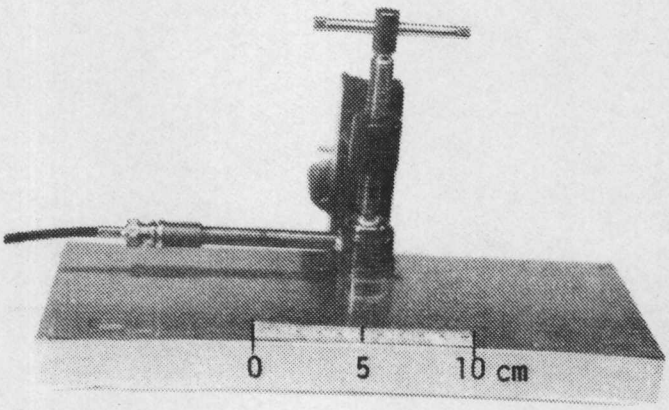


Figure III-2. Ultrasonic Measurement Setup Showing the Steel Plate, the Transducer, and the Vise.

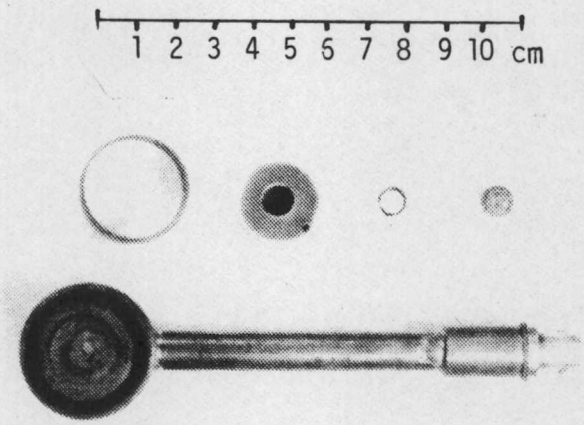


Figure III-3. Transducer Parts. Top row, left to right: lucite crystal housing ring, lucite cylinder housing, contact spring, contact cylinder. Bottom row: main brass housing.

depression has an inside radius 1 mm smaller than the crystal radius and an outside radius of about the size of the crystal so that the crystal can be inserted in this depression. Since the depth of this depression is smaller than the thickness of the crystal, the pressure applied on the housing is uniformly distributed on a 1 mm ring at the rim[1] of the crystal. It was necessary to use pressure and wring the crystal on the surface for two main reasons. First, it was a simple yet efficient way to ensure parallelism between crystal and sample faces. As pointed out by Truell et al. (1969), "ordinary bonding techniques do not necessarily provide sufficiently good control over parallelness" (p. 120). Furthermore, the effect of nonparallelism of sample faces is almost impossible to differentiate from the effect due to lack of parallelism between the crystal and the sample faces. Secondly, to wring the crystal on the surface is a very efficient way to damp the crystal and avoid the "ringing" effect described by Krautkramer (1977). In this case the cohesive force between the sample and the crystal allows the sample itself to act as damping material. This negates the need for rubber backing, the usual damping material, which causes a significant decrease of crystal sensitivity.

b. Electrical circuit. The electrical signal from the decoupler enters at the BNC connector of the main housing. It is then fed through the central spring loaded retractable connector. This connector is in

---

[1]By applying the pressure at the rim of the crystal rather than at the center, uneven loading of the crystal was avoided as well as unnecessary loss of sensitivity to returning echoes.

contact with a brass cylinder. This cylinder can move up and down within the lucite cylinder housing which fits into the center of the crystal housing ring. The cylinder is spring loaded by a central connector, located inside the brass housing, so that it stays in contact with the electrode attached to the surface of the crystal. Two types of electrodes are used: gold and silver.[1] The electrical circuit is then completed by connecting the lower face of the crystal to the brass housing. This is achieved by connecting the sample to the brass housing using a brass connector.

3. Sample

The sample used is a plate of high carbon steel. This material was selected for its known characteristics of: isotropy, low attenuation coefficient from 2 to 5 MHz, electrical conductivity and machinability. The plate geometry is necessary to eliminate side effects which can easily be confused with nonparallelism effects as noted by Truell et al. (1969), and to facilitate machinability of specified angles.

The plate was first ground to ensure parallelism of upper and lower faces and to eliminate surface defects larger than 1×10^{-2} cm (this represents about one-tenth of the wavelength at 6 MHz). The upper plate was then ground in facets of approximately 3 cm in width. A drawing showing the approximate geometry and the coordinate system used is shown in Figure III.4. The z direction corresponds approximately to

---

[1] A gold electrode was plated on the entire (1.27 cm-radius) crystal surfaces. For the 7 MHz crystal only, a 1.14-cm partial aluminum electrode was attached by a grease couplant which was squeezed as thin as possible. Such partially-plated transducers have been studied by Papadakis (1975).

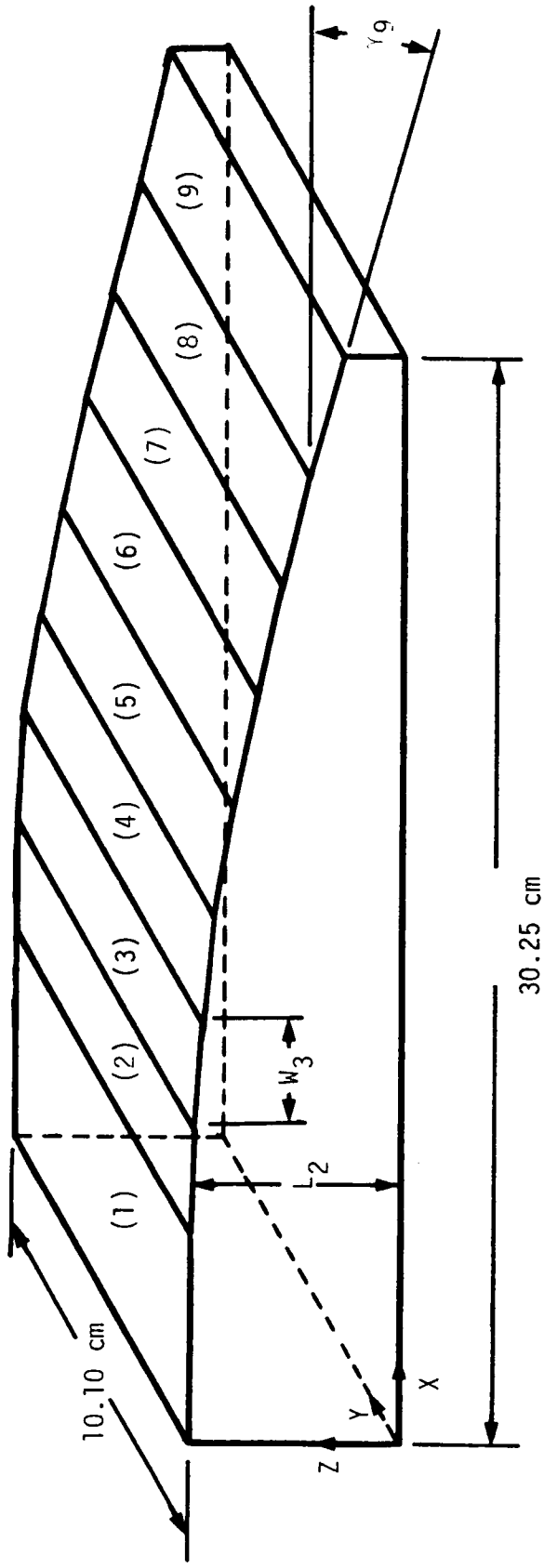


Figure III.4. Geometry of the Wedged Sample.

the propagation direction of the echoes, the y direction corresponds to the width of the sample and the -x direction corresponds approximately to the direction of lateral displacement of the propagating wave. As we go along the x direction, we note an increase of the relative angle between the upper facets and the lower face. This relative wedge angle (γ) increases from 0 to 45 minutes by increments ranging from 20 seconds to about 15 minutes. The width W_n of the facets ranges from 3 to 5 cm.

C. EXPERIMENTAL PROCEDURE

1. Sample Characterization

a. Angles measurements. The angles between the lower face and each facet is evaluated by using a collimator and two reflectors as shown in Figure III.5. The collimator and the first reflector are positioned such that the cross hairs' image coming from the lower face reflector is coincident with the micrometer cross hairs. The micrometer cross hairs' position is noted. The second reflector is now positioned at the edge of the facet of the upper face to be measured and the micrometer cross hair positioned to be coincident with the image from this upper face reflector. Since both reflectors have parallel and flat faces and have one or part of one of their faces wrung onto the sample, the wedge angle (γ) between both faces is given by:

$$\gamma = \frac{\sin^{-1}(\Delta x/f)}{2}$$

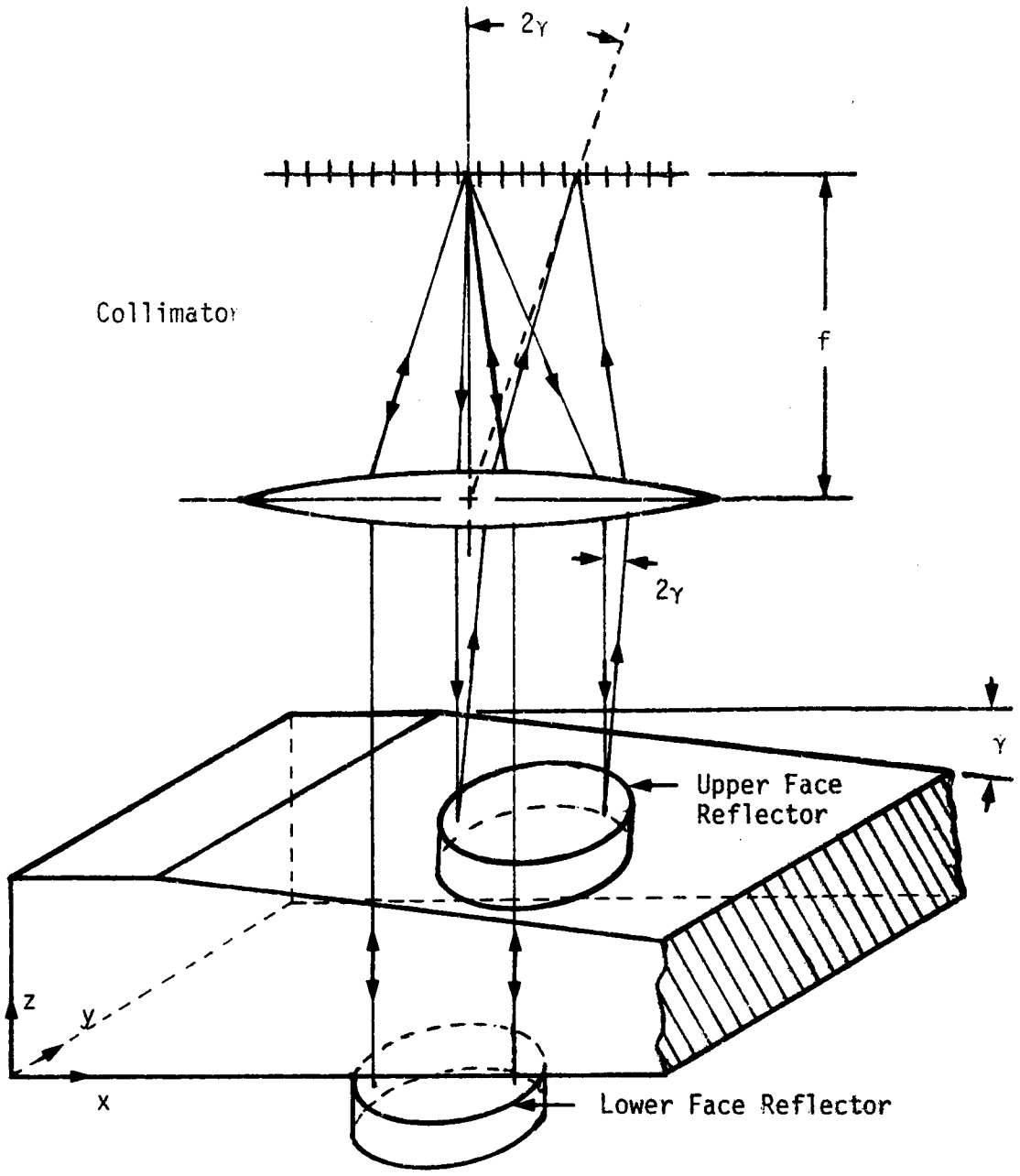


Figure III.5. Schematic of Optical Measurement Setup.

where

γ = wedge angle;

f = focal length[1] of the collimator = 33.23 mm;

Δx = distance between the two image positions along the x axis.

The distance L_n is the sample length measured between the lower end and the upper facet n. Four measurements were made at each facet: γ_n at both edges of the sample (y = 0 cm and y = 10.5 cm) and L_n at about 3 cm from either edge of the sample (y = 3 cm and y = 7 cm). The position of y for measurements of L_n correspond approximately to the position of the center of the transducer. The result of these measurements is shown in Table III.1.

b. Velocity measurement. The measurement of velocity is made by using a method analogous to the long pulse technique described by McSkimin (1950). First, the facet used for measurements is thoroughly[2] cleaned with acetone. The crystal is then positioned at the center of this facet on a drop of couplant[3] squeezed between the crystal and the sample to ensure a good mechanical coupling. The transducer housing

---

[1]The value of f, the focal length, was measured using the Newtonian method described by Palmer (1969).

[2]The cleaning is extremely important, as it prevents lack of parallelism or bad coupling due to the presence of dust particles.

[3]After many trials, nonaq stopcock grease was selected as couplant. Its chief advantage is that when pressure was applied, an even and very thin layer of couplant was formed. This permitted to wring the crystal very easily on the sample and the ultrasonic transmission properties of this coupling were excellent. Another advantage is that the crystal could afterwards be easily removed by sliding it to the edge of the sample.

TABLE III.1

SAMPLE GEOMETRY DATA[a]

n	γ_n (milliradians)[b]		L_n (cm.)[c]	
	y = 0.0 cm	y = 10.0 cm	y = 3.0 cm	y = 7.0 cm
1	0.14	0.14	2.4845	2.4845
2	0.11	0.19	2.4855	2.4855
3	0.00	0.00	2.4856	2.4865
4	0.27	0.16	2.4860	2.4865
5	0.28	0.00	2.4860	2.4865
6	1.60	1.62	2.4845	2.4850
7	3.82	3.87	2.4773	2.4775
8	8.75	8.07	2.4563	2.4570
9	11.64	11.75	2.4243	2.4280

[a]The variations of γ_n and L_n observed along the y direction were caused by machining problems.

[b]Accuracy of the measurements, $\pm 3 \times 10^{-2}$ milliradians.

[c]Accuracy of the measurements, $\pm 5 \times 10^{-5}$ cm.

is then mounted on the crystal and the pressure slowly increased by tightening the vise. During this operation the RF pulse rather than the boxcar integrator gate position is monitored on the oscilloscope. (This connection is shown as a dotted line on the block diagram of Figure III-1, p. 37.) When the RF[1] and rectified pattern, as seen on the oscilloscope, show no signs of distortion and when increasing the pressure does not improve the pattern, the boxcar integrator gate position indicator output is reconnected to the oscilloscope. At this point the transducer setup is complete and the measurement procedure is started.

The exact fundamental frequency of the crystal is first evaluated by changing the frequency on the VFO until minimum attenuation of the last echoes is observed. The frequency is then read on the frequency counter. The length of the pulse is increased until overlap of successive echoes occurs. The frequency of the VFO is then changed by about 1 MHz on either side of the crystal fundamental frequency (f_o). As the frequency changes, interference minima and maxima are observed. The gate of the boxcar integrator is positioned at the overlap of the second and the third echo. The number of minima between the highest and the lowest frequency is then noted and the values of these two frequencies are read from the frequency counter. The velocity v is given by:

$$v = 2 \times L \times \Delta f$$

---

[1]For the velocity measurements the RF was set at 4 MHz which was approximately the fundamental frequency of the crystal used for measurements.

where L is the sample length and Δf is the change in frequency between two "in phase" conditions of the second and third echo. To improve the accuracy of the velocity value 21 sets of measurements of about 15 minima each are taken. The average velocity ($\tilde{v}$) obtained is 0.5840 cm/μsec with a standard deviation of 0.5%. An approximate calculation of the effect of the phase change caused by the relative magnitude of the crystal and the sample mechanical impedance is shown in Appendix C. The result is that this correction in this case is negligible.

2. Attenuation Measurements

The procedure used for attenuation measurements is the same as the one used for velocity measurement up to and including the fundamental frequency determination. The range of usable frequency is 3 to 9 MHz. The frequencies used are all higher than 3 MHz to eliminate two problems. First, an impedance mismatch between the pulser and the transducer (this mismatch is an inverse function of the frequency); and second, an increasingly difficult mechanical coupling of the crystal to the sample, as the thickness of the crystal is increased. No frequencies higher than 9 MHz can be used as the increase of attenuation of the ultrasonic wave in the sample prevented measurement of a sufficiently large number of echoes.

Once the resonant frequency is defined, the pulse parameters are adjusted to give pulses and echoes with minimum distortion (flat top) and which show no sign of interfering with each other. The width of the gate is then set so that it could cover only the flat top part of any echo. The first echo is then set at a given reference level

(2 or 5 volts) and all the other echoes' amplitude measured by the boxcar integrator. The reference setting is checked regularly to ensure the validity of the relative amplitude measurements. The transducer and the crystal are then removed and the measurement repeated on another facet.

CHAPTER IV

RESULTS AND CONCLUSIONS

A. EXPERIMENTAL RESULTS

1. The Amplitude Pattern

A series of amplitude measurements was made in accordance with the procedure described in Chapter III. These measurements were made for 34 different combinations of four parameters: (1) frequency (f), (2) wedge angle (γ), (3) sample length (L), and (4) radius of the piezoelectric element (a).

Figure IV-1 shows an example of exponential decay pattern observed on the CRO. These patterns were observed when the wedge angle was small enough and the frequency low enough. In other cases in which the frequency was high enough and the wedge angle large enough significant fluctuations about the exponential decay patterns were observed. A photograph of one of these fluctuating amplitude decay patterns, as seen on a CRO, is shown in Figure IV-2. A plot of such fluctuating amplitudes is shown in Figure IV-3.

2. The Attenuation Parameter

The attenuation parameter α is the quantity that is modified in the course of this study to bring it closer to the ultimate goal α_i. The parameter α is given by Eq. (2-6):

$$\alpha = \frac{20}{\Delta x} \log_{10}\left(\frac{P_0}{P(x)}\right) .$$

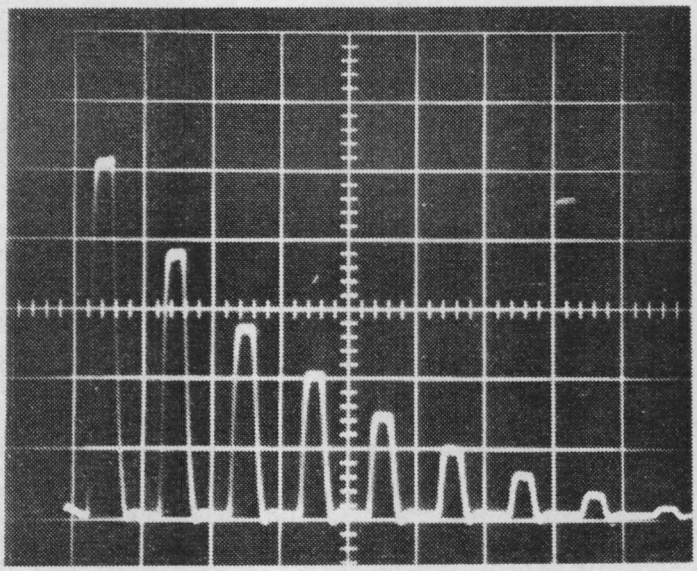


Figure IV-1. Exponential Decay Pattern at 6 MHz for 0 Wedge Angle.

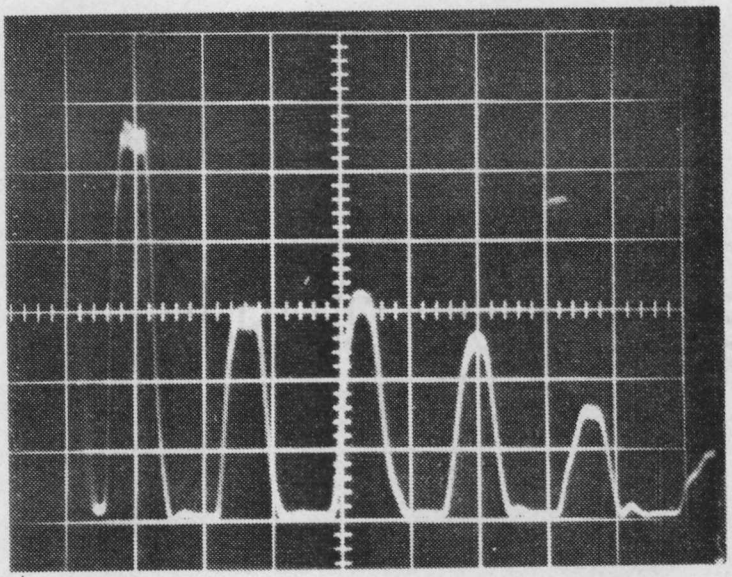


Figure IV-2. Fluctuations in the Echo Pattern Observed at 3 MHz for $\gamma = 11.75 \times 10^{-3}$ Radians.

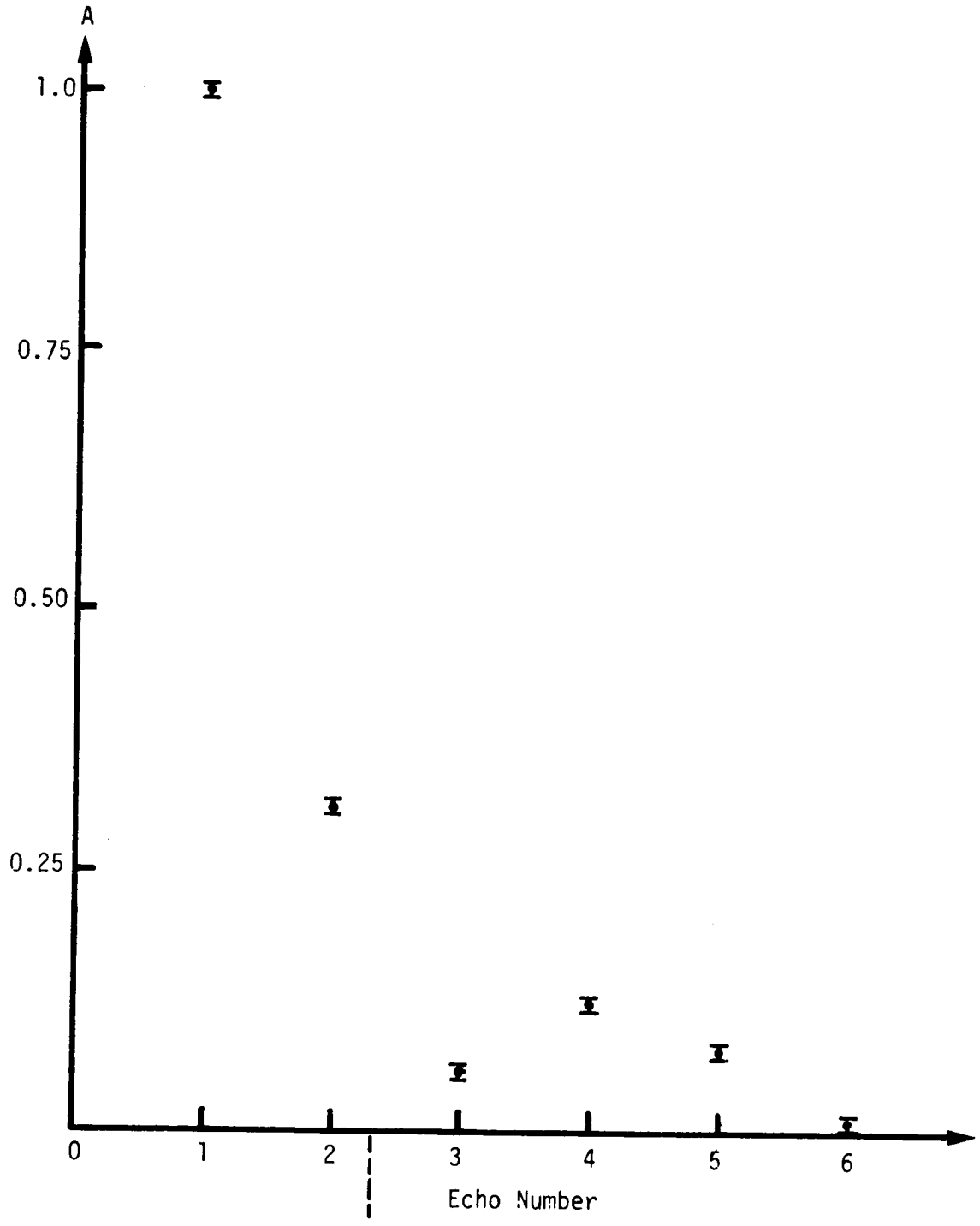


Figure IV-3. Pulse Amplitude Pattern at 4 MHz for a Wedge Angle of 11.75 x 10^{-3} Radians.

In our study we will use P_0 as the amplitude of the first measured echo and P(x) as the amplitude of the nth echo. Then Δx, the propagation path from echo 1 to echo n, is given by:

$$\Delta x = (R_0)_n - (R_0)_1$$

where $(R_0)_n$ is the distance between the center of the receiver and the source after n reflections and is given by Eq. (2-42). Values of α are calculated by the computer program in Appendix B and are given by the variable DBMP. When we use the uncorrected data, this parameter represents the apparent attenuation. Some plots of apparent attenuation versus n obtained at 4 MHz and 7 MHz for various wedge angles are shown in Figures IV-4 and IV-5. The plots show that (1) the apparent attenuation is a strong function of the wedge angle and the echo number; (2) for higher frequency the attenuation parameter becomes sensitive to smaller variations of wedge angle and echo number; and (3) the echo trains exhibit both variations (monotonic increases) and fluctuations (somewhat periodic changes).

B. THE DIFFRACTION CORRECTION

The diffraction correction defined by Eq. (2-21) can be applied to amplitude values obtained on facets with zero wedge angles. A corrected attenuation value can then be obtained by using these corrected amplitude values in Eq. (2-6). This corrected attenuation is evaluated by the computer program in Appendix B and is given by the variable DBCD. A plot of both the apparent and corrected attenuation

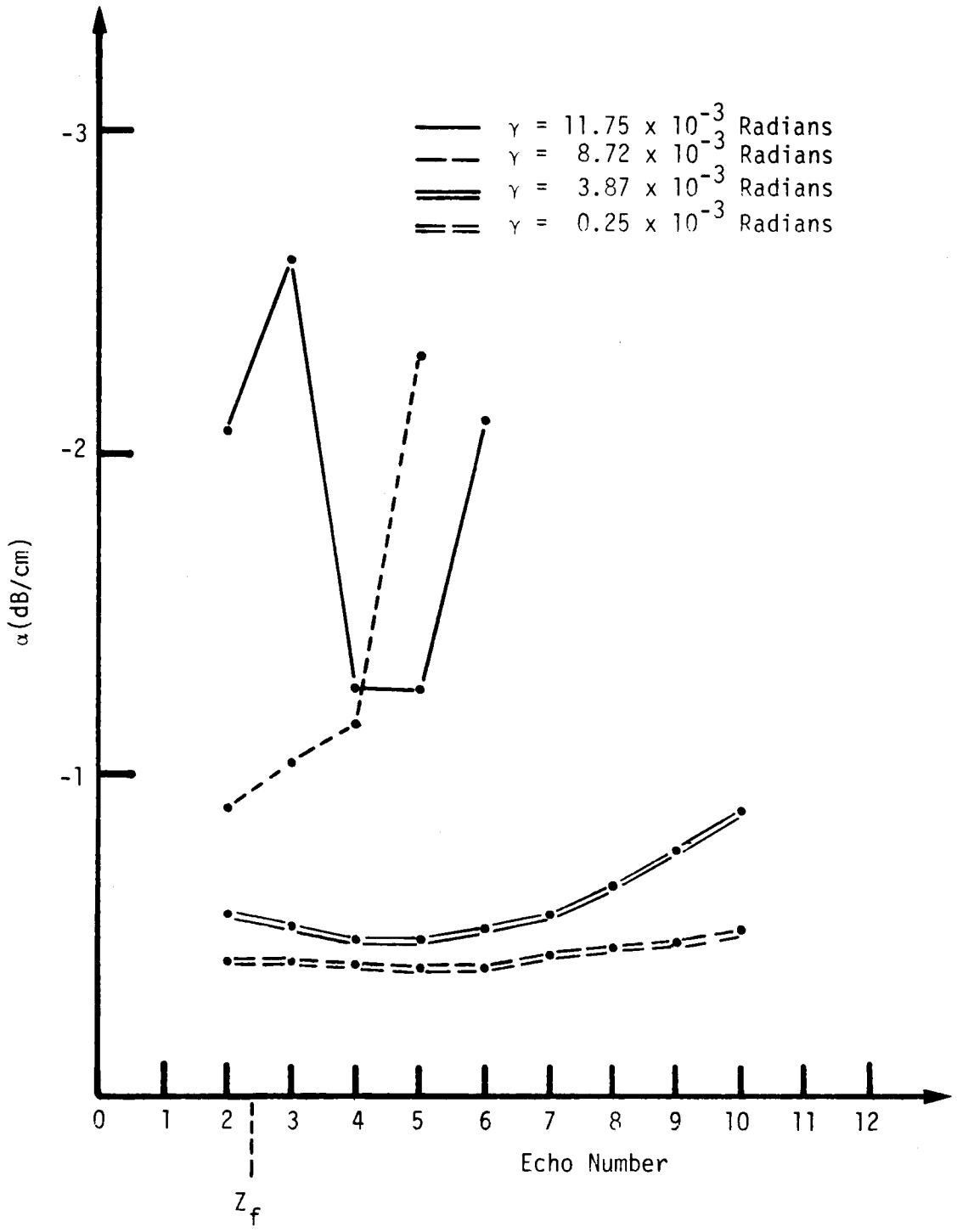


Figure IV-4. Apparent Attenuation at 4 MHz for Different Wedge Angles.

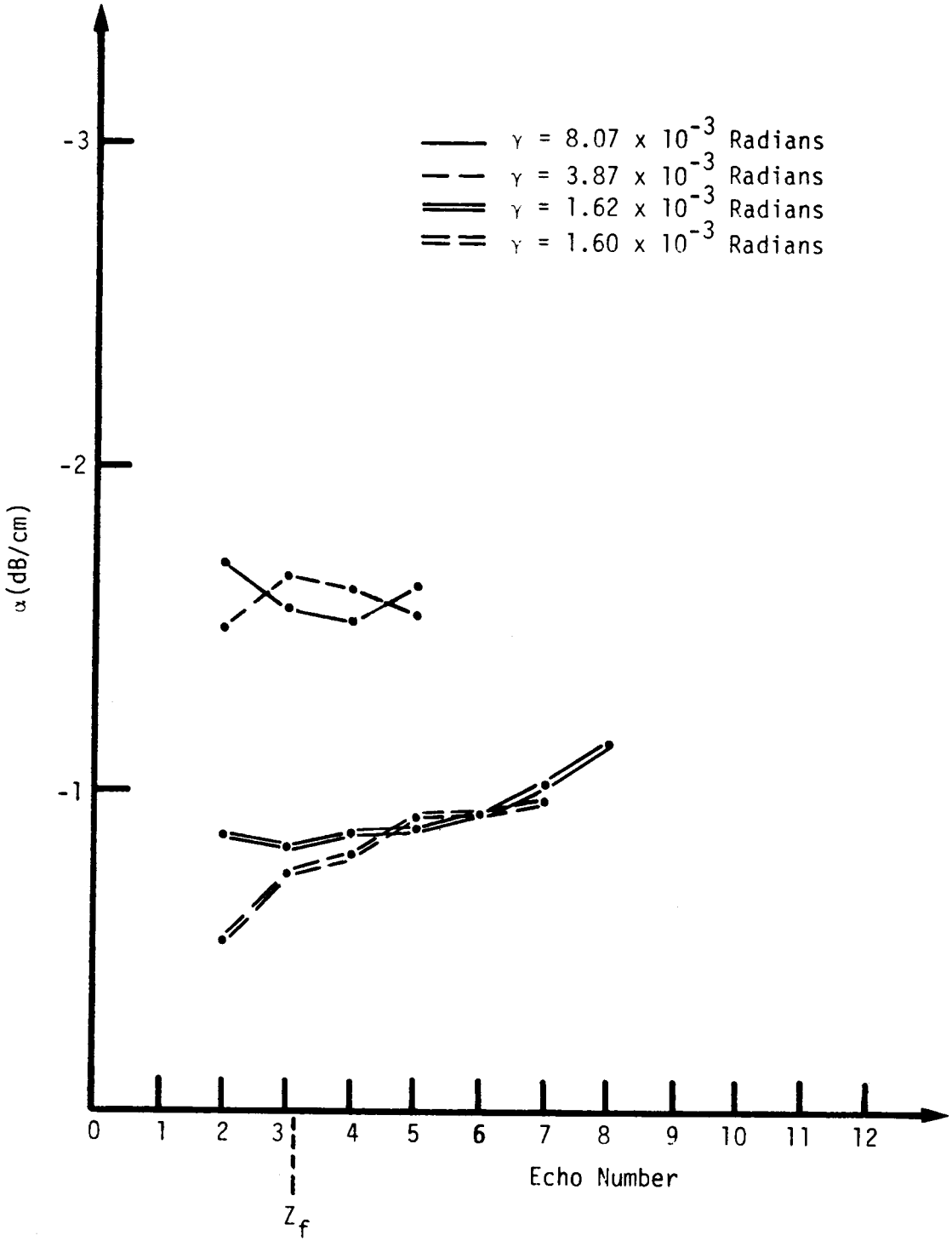


Figure IV-5. Apparent Attenuation at 7 MHz for Different Wedge Angles.

as a function of the echo number for data taken at 3.34 MHz is shown in Figure IV-6. A similar plot for data taken at 6 MHz is shown in Figure IV-7. The plots show that the corrected attenuation has a smaller magnitude than the apparent attenuation. For the first two echoes at 6 MHz and for the first six echoes at 3 MHz variations of apparent attenuation are larger for smaller frequencies than for larger frequencies in contrast with the effect of the change in wedge angle. (The change in wedge angle resulted in larger variations for higher frequencies.) These variations are corrected for by the diffraction correction and a reference attenuation is plotted by taking the average of these first few corrected echoes. Dotted lines giving the reference attenuation are given in Figure IV-6 and succeeding figures.

Deviation of the data from the reference attenuation for the later part of the echo train cannot be explained by this correction model for two reasons. First, even though the approximations of the model should be better and better as n increases (Rogers and Van Buren (1974) report an accuracy of at least 0.6% in the Fresnel zone for the range of values of ka used here), the deviation of the corrected attenuation from the reference attenuation becomes larger and larger as n increases. Second, in contrast with the prediction of this correction model, the deviation of the attenuation data from the reference attenuation is larger for high frequency than the deviation of the data observed for low frequency. The possibility of having inhomogeneity in the sample, which would give a pattern similar to non-parallelism, was reported by Truell et al. (1969). However, we believe that the quality of the sample is such that this possibility seems

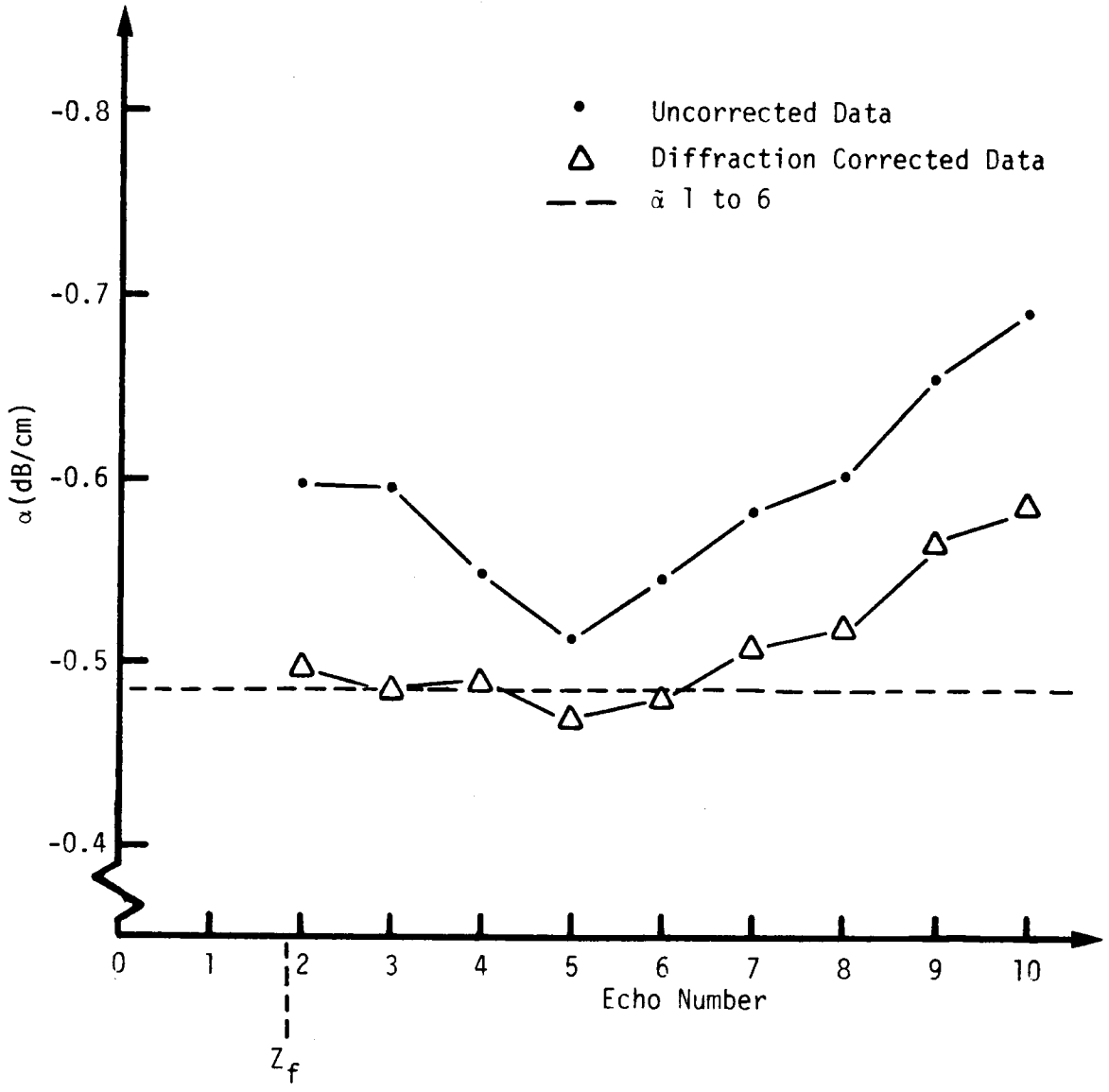


Figure IV-6. Attenuation at 3.34 MHz for 0 Wedge Angle. A Reference Attenuation is Obtained by Averaging the First Six Echoes.

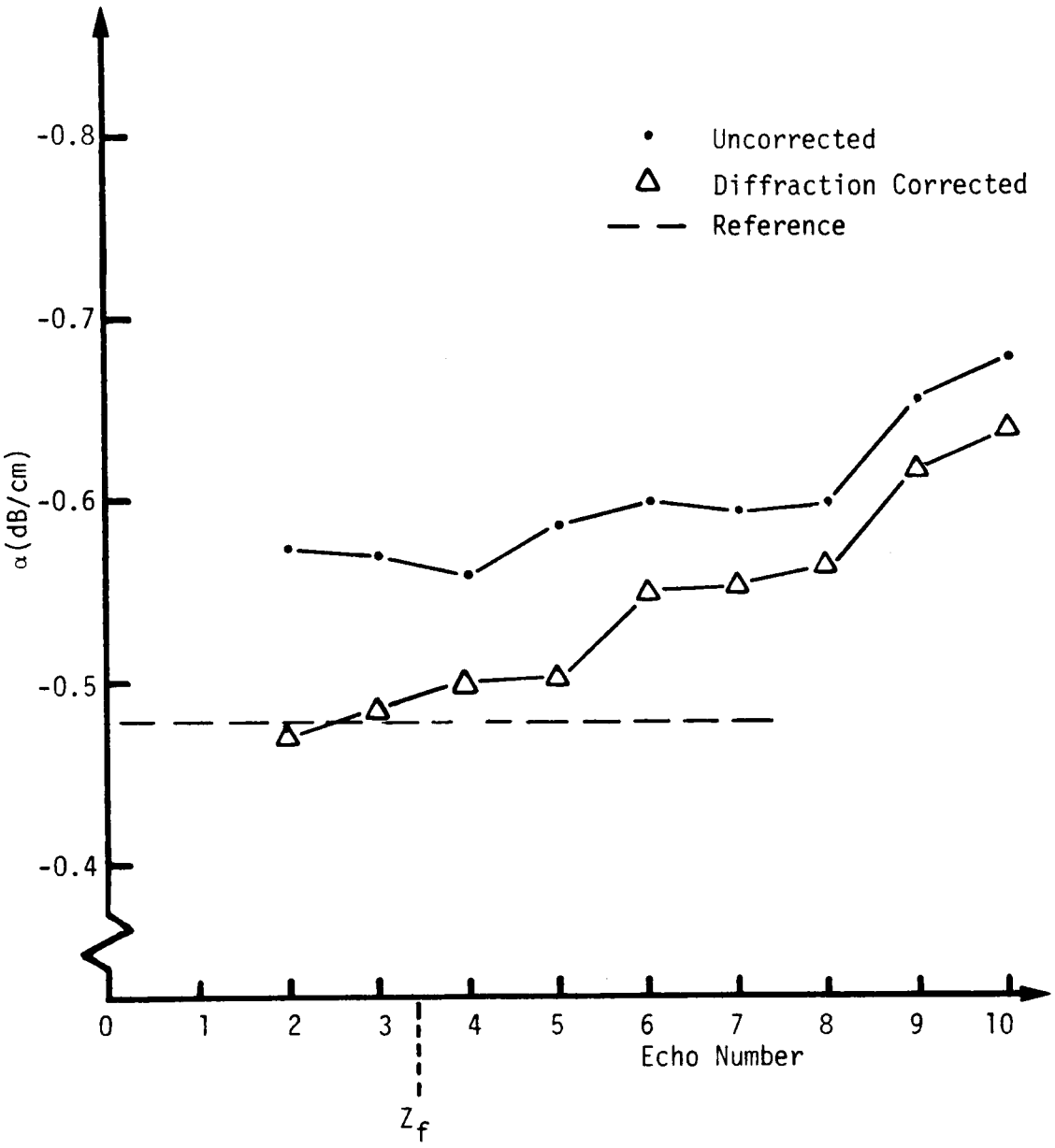


Figure IV-7. Attenuation at 6.00 MHz for 0 Wedge Angle.
A Reference Attenuation is Obtained by Averaging the First Two Echoes.

unlikely. However, this pattern is very similar to the results of varying wedge angles. The accuracy of wedge angle measurements was limited to 3×10^{-5} radians. If we now assume that a wedge angle of 2×10^{-5} radians is present here, then (from Eq. (2-22)) after three reflections the incident angle of the wave on the receiver will have a magnitude comparable to the smallest wedge angle in the sample. A conclusion which could then be drawn from the behavior of the later part of the echo train is that, given enough reflections, the data seem to be more sensitive to wedge angle variations than the optical measurement method described in Chapter II.

These studies, then, allow us to make two important statements. First, for extremely small angles the early part of the echo train allows one to conclude that the diffraction correction is valid for up to six echoes at frequencies as low as 3 MHz, and up to two echoes for frequencies as high as 6 MHz. Second, the later part of the echo train follows the behavior predicted for any wedged sample: γ_n, the effective incident angle of the receiver, increases at each reflection so that for higher frequencies the smaller wavelength makes the deviation from an exponential echo train more noticeable.

C. APPLICATION OF THE PLANE WAVE GEOMETRICAL CORRECTION

It is clear from Figures IV-4 and IV-5 that the magnitude of the apparent attenuation is strongly influenced by the value of wedge angle. Since the diffraction correction does not take into account the change in wedge angle, an attempt is made to solve this problem by the use of the Truell and Oates correction function $H(\gamma_n)$ given in Eq. (2-27).

The amplitude values are first corrected for diffraction. From these values, a diffraction corrected attenuation (given by DBCD in Appendix B) is obtained. Then the diffraction corrected amplitude values are recorrected by using the Truell and Oates correction function. The attenuation obtained from these recorrected values (given by DBCPG in Appendix B) will be referred to as attenuation corrected for plane wave geometry. The plane wave correction model is now applied to fluctuating patterns such as the one shown in Figure IV-3 (p. 55). The diffraction corrected attenuation as well as the attenuation corrected for plane wave geometry are shown in Figure IV-8. As can be seen from these plots when the fluctuations of attenuation values are fairly large, as long as the propagation path is less than 2 Z_f, the plane wave model corrects in the right direction. However, in these cases it significantly overcompensates for the fluctuations. Examination of the data reveals that this model improves the prediction of the shape of the fluctuations as we get closer to the Fresnel zone or, equivalently, as the pressure distribution on the receiver approaches the plane wave model. This correction was applied to different combinations of frequency and wedge angle and in most cases it overcompensated for large wedge angles and undercompensated for small wedge angles.

Calder showed that his correction was quantitatively inappropriate for his measurements in solid helium. The results presented above agree with Calder. Even though the Truell and Oates model gives the approximate shape of the observed fluctuations, it is not possible to use it for quantitative corrections in our case.

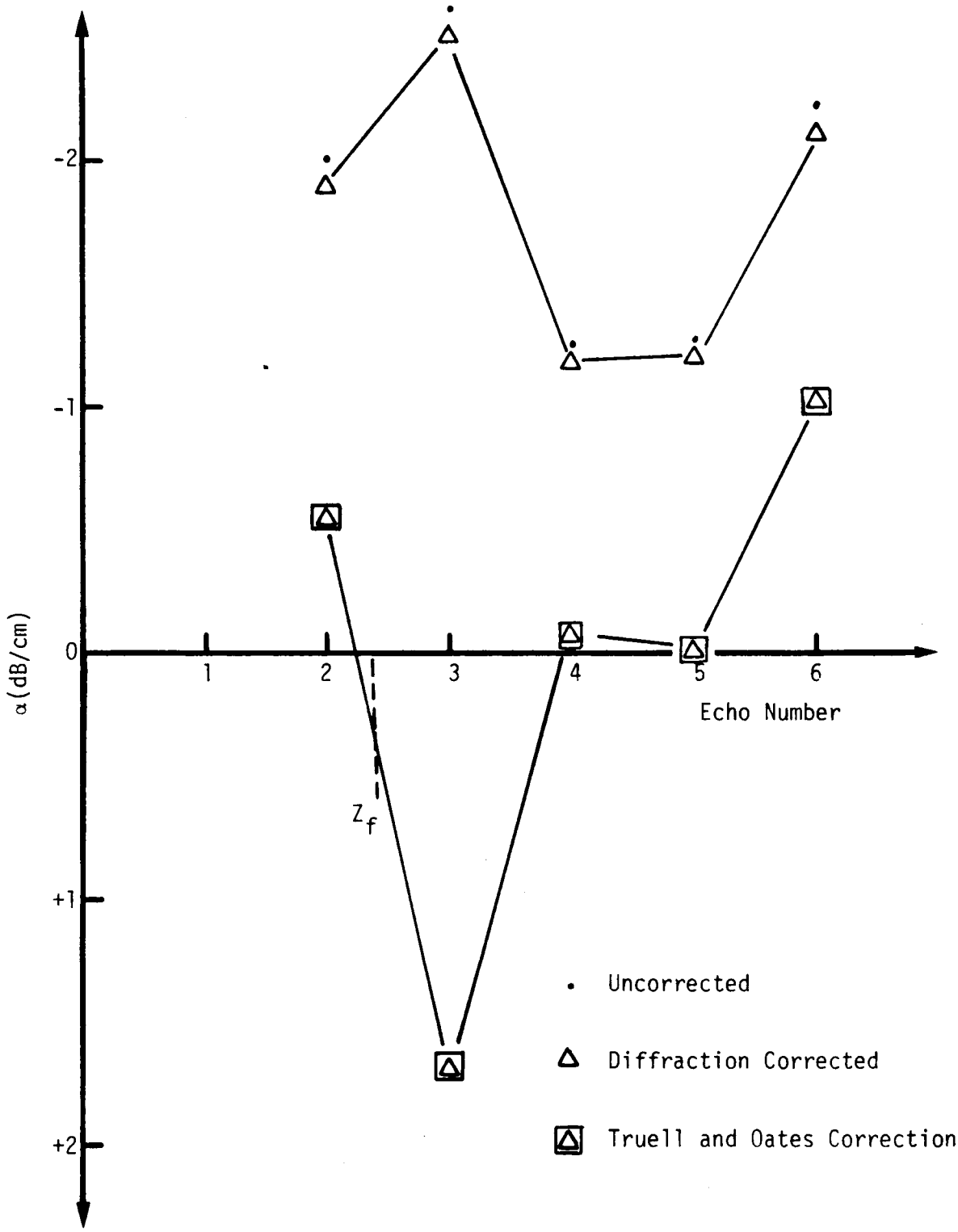


Figure IV-8. Attenuation at 4 MHz for a Wedge Angle of 11.75×10^{-3} Radians Using the Truell and Oates Correction.

D. APPLICATION OF THE DIFFRACTED WAVE GEOMETRICAL CORRECTION

The diffracted wave geometrical correction is now applied to the uncorrected farfield data and the values of $\alpha(n)$ (given by the variable DBCDG in Appendix B) versus n are plotted. For comparison in the far-field and to allow for partial correction in the Fresnel zone, the diffraction correction also is given.

Such corrections to the data shown in Figure IV-3 (p. 55) are plotted in Figure IV-9. The diffracted wave geometrical correction brings the values much closer to the values observed for smaller wedge angles in Figure IV-4 (p. 57). In Figure IV-9 one observes that the correction gives more consistent results than the two previous corrections and brings the corrected values closer to the values obtained for smaller wedge angles in the region in which fluctuations occur. For some specific combinations of relatively large frequency and wedge angles, such as the one shown in Figure IV-10 for data taken at 5.75 MHz, this geometrical correction successfully corrects the apparent attenuation such that the corrected attenuation closely approximates the reference attenuation value obtained for zero wedge angle at approximately 6 MHz. In general, for the frequencies in the 4 to 6 MHz range and wedge angles smaller than 3.82×10^{-3} radians, the correction brought at least the first one or two echoes of the far-field into the range predicted from the reference attenuation obtained for smaller wedge angles.

In Figure IV-11 a plot of the corrected data at 3.13 MHz for a wedge angle of 3.82×10^{-3} are shown. As can be seen from the plot,

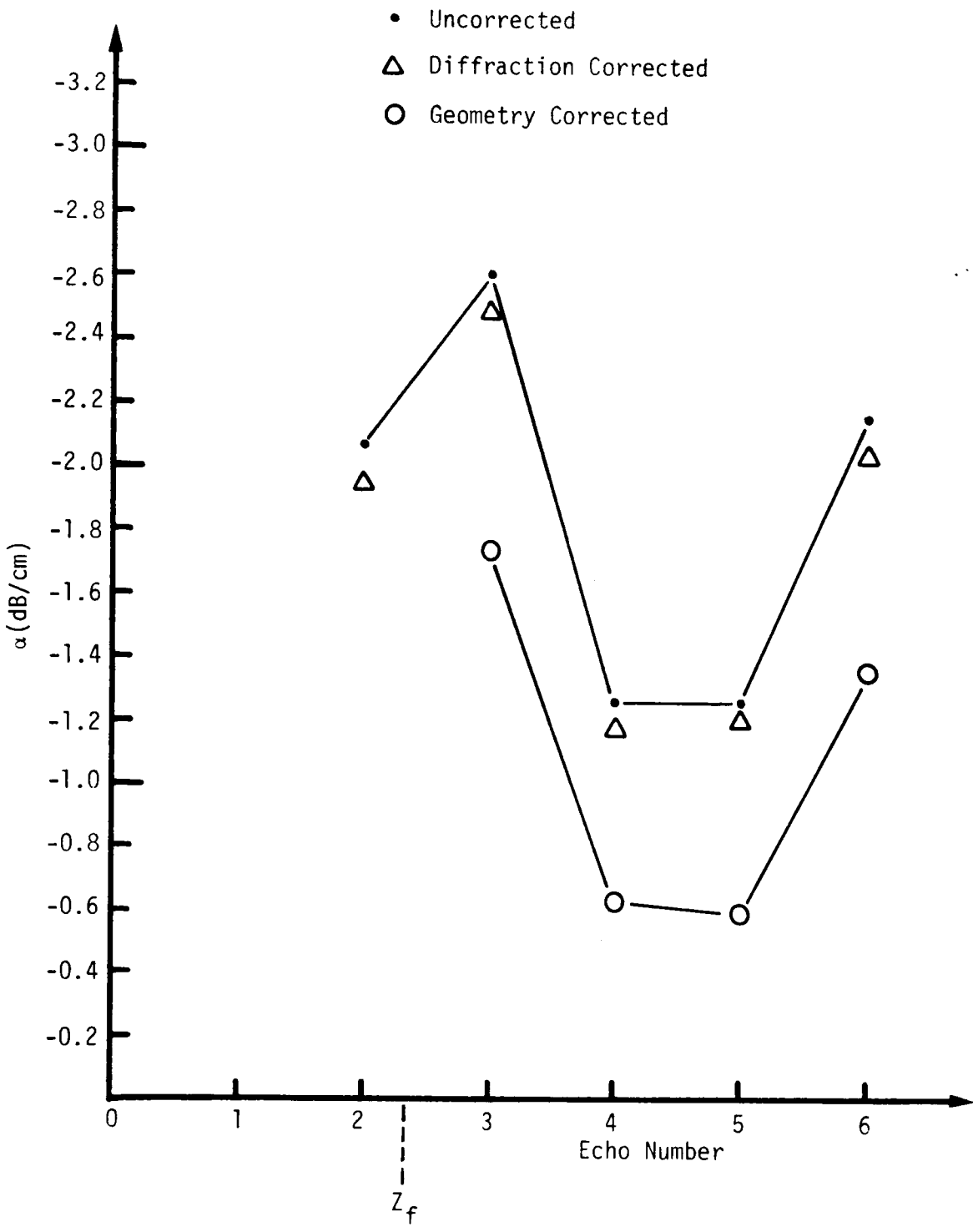


Figure IV-9. Attenuation at 4 MHz for a Wedge Angle of 11.75×10^{-3} Radians Using Data Corrected for Diffracted Wave Geometry.

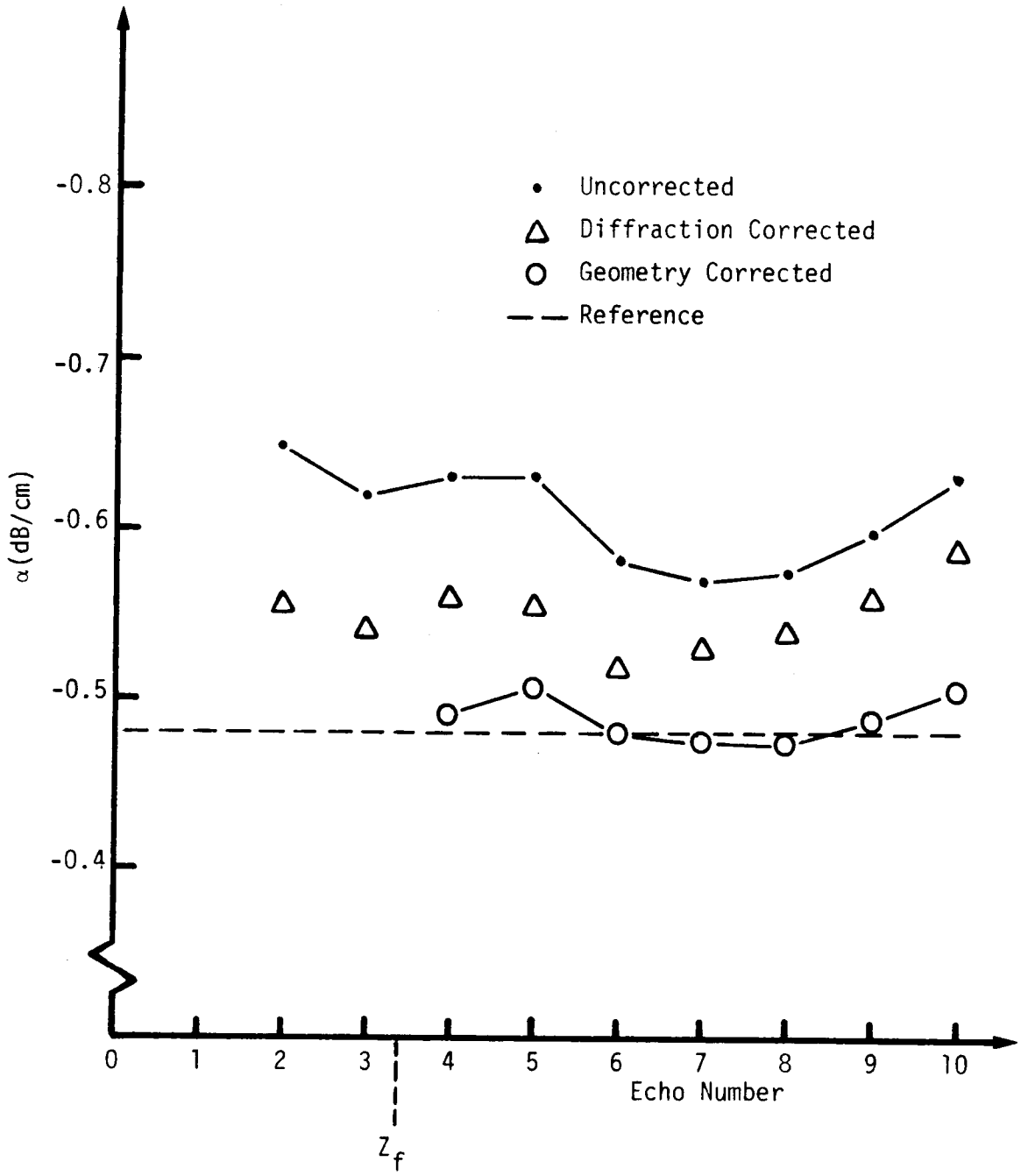


Figure IV-10. Attenuation at 5.75 MHz for a Wedge Angle of 3.82×10^{-3} Radians Using Data Corrected for Diffracted Wave Geometry and Reference Attenuation for $\gamma = 0$ and f = 6 MHz.

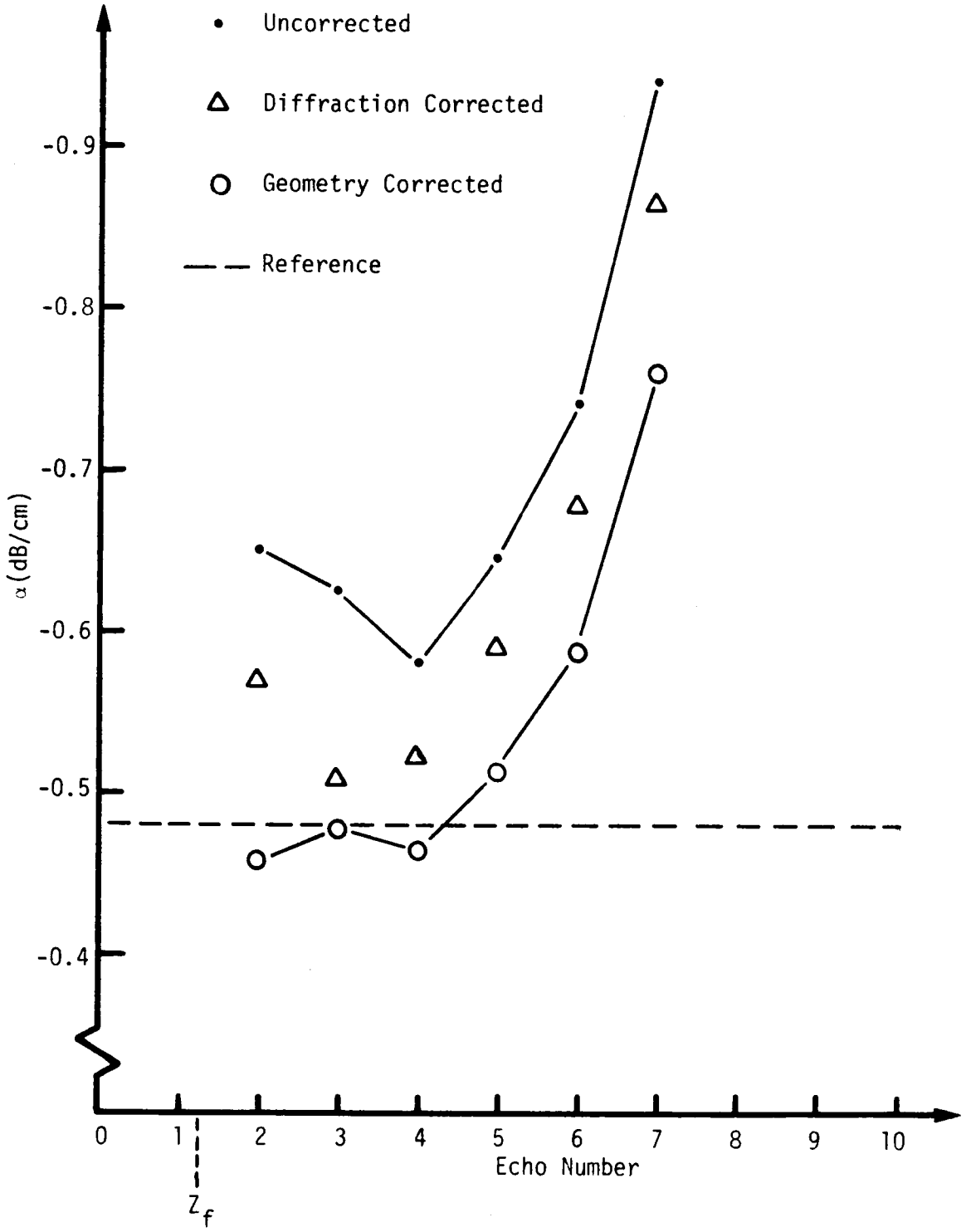


Figure IV-11. Attenuation at 3.13 MHz for a Wedge Angle of 3.82×10^{-3} Radians Using Data Corrected for Diffracted Wave Geometry and Reference Attenuation for $\gamma = 0$ and f = 3.34 MHz.

the corrected reference attenuation, at least for the first few echoes, gives a close approximation of the reference attenuation line. The correction also was applied at 4 MHz to angles of 3.82×10^{-3} radians or smaller and in all cases the corrected values of the first one to three echoes were within 5% of the reference attenuation obtained at lower wedge angles.

In summary, the important points are that (1) for frequencies higher than 4 MHz this model corrects partially for the deviation from the reference attenuation when the type of fluctuations shown in Figure IV-9 do not occur, i.e., for relatively low wedge angles; and (2) if the frequency is 4 MHz or lower, then our model successfully corrects for geometrical attenuation (at least for the first few echoes) even for wedge angles as large as 3.82×10^{-3} radians.

E. CONCLUSIONS

From the analysis of the data reported here two main conclusions seem to emerge.

1. The large fluctuations and variations observed when either the wedge angles or the echo number were large enough or the frequency high enough, cannot be explained entirely on the basis of the diffraction model used here. Even though the neglect of the beam displacement and of the actual pressure distribution seems to invalidate the Truell and Oates plane wave model in our situation, the results show that the Truell and Oates function $H(\gamma_n)$ does, in contrast with the other corrections, take into account the form of the large variations

and fluctuations at least when the shape of the wavefront approaches the plane wave approximation.

Kinsler et al. (1982) gave a description of similar fluctuations and variations. They attribute these fluctuations and variations to a receiver directivity factor $H_r(\theta_i)$, where θ_i is the incident angle of the wave on the transducer. According to Kinsler, the receiver directivity factor $H_r(\theta_i)$ is given by the magnitude of the directivity function $H(\theta)$ of the receiver when used as a transmitter. A mathematical justification of this statement is shown in Appendix D. Then if a plane wave is impinging on a receiver $H_r(\theta_i)$ will be given by the magnitude of the directivity function of a piston source. If we now take the magnitude of the directivity function of a piston source given in Eq. (2-20) we obtain the Truell and Oates function $H(\gamma_n)$ given in Eq. (2-26) since γ_n gives the magnitude of θ_i. Then in our case the value of the Truell and Oates function seems to reside in the fact that it has exactly the same form as the receiver directivity function for a plane wave impinging on a circular receiver.

We are then led to the conclusion that when the wedge angle or the echo number is large enough or the frequency high enough, both the geometrical attenuation and the receiver directivity significantly affect the measured attenuation. And, in our case, the model of the receiver directivity factor based on the plane wave assumption can only be used in a qualitative manner. The important point, however, is that the model of the receiver directivity factor gives a plausible physical explanation of the large fluctuations and monotonic variations observed in the echo train.

2. From the analysis of our data it appears that a geometrical correction should be applied to all the amplitude measurements made on wedged samples when the intrinsic attenuation is desired. Only the cases when the wedge angle is so small that it cannot be detected by a method of accuracy comparable to the one used here, is it sufficient, at least for frequencies lower than 6 MHz and for the first few echoes, to use the diffraction correction for parallel faces as geometrical correction. In all the other cases the diffracted wave geometrical correction should be used.

In some cases the geometrical correction is the most significant correction and the receiver directivity factor can be neglected. These are characterized by the fact that the values of amplitude corrected for geometrical attenuation gives an approximately constant intrinsic attenuation. In our experiments they occurred mainly at frequencies lower than 4 MHz and for wedge angles smaller than 3.82×10^{-3} radians.

F. SUGGESTIONS FOR FURTHER WORK

1. Receiver Directivity Factor

Probably the most significant improvement to the correction for nonparallelism would be the definition of a receiver directivity factor which could be applied to cases for which the plane wave assumption is not satisfied. As a secondary investigation, a calculation of the directivity function in the farfield of a circular source having a distribution of the form $2J_1(r)/r$ was made. The results show that a considerable decrease in the amount of overcompensation for the receiver effects is obtained when this directivity function is used for

correction. Further investigation along this direction probably would be fruitful.

2. Correction in the Fresnel Zone

A very useful improvement of the diffracted wave geometrical correction would be to extend its validity farther into the Fresnel zone. This would allow for correction in a region which is commonly encountered in nondestructive testing situations. The mathematical difficulty associated with this improvement is a long-standing impediment to solution of all diffraction problems.

3. The Gaussian Transducer Model

During the course of this investigation it became clear that an analytical solution based on a radiating element with a diffraction field showing radial symmetry would be difficult to handle. This is the reason a numerical solution was used. An experimental configuration which would lend itself to the use of cartesian coordinates would be much simpler to model mathematically. The Gaussian transducer developed by Martin and Breazeale (1971) has this characteristic.

A theoretical solution of the problem of evaluating the diffraction field of a Gaussian transducer is included in Appendix E. Experiments modeled on this solution would be very interesting.

4. Velocity Measurements

As can be seen from Figures II-9 and II-10 (pp. 26 and 29), if the wedge angle or the sample length is large enough significant variations in the measurements of velocity will occur because of the

variations in the propagation path between echoes. Preliminary results obtained in large steel blocks (20 cm) with large wedge angles (1 to 2°) at a frequency of about 5 MHz showed that significant decreases (up to 5%) can be observed in the transit time between two successive echoes. A study of the variation of velocity measurements in wedged samples promises to be an interesting field of investigation.

LIST OF REFERENCES

LIST OF REFERENCES

Abramowitz, M. and I. A. Stegun, eds. Handbook of Mathematical Functions. Appl. Math. Ser. No. 55. Washington, D.C.: Government Printing Office, 1972.

Benson, G. C. and O. Kiyohara. J. Acoust. Soc. Am. 55, 184 (1974).

Breazeale, M. A., John H. Cantrell, Jr., and Joseph S. Heyman, "Ultrasonic Wave Velocity and Attenuation Measurements," Chap. 2 in Methods of Experimental Physics, Vol. 19, edited by Peter D. Edmonds. New York: Academic Press, 1981.

Calder, I. D. J. Acoust. Soc. Am. 63, 967 (1978).

Gray, A., G. B. Mathews, and T. M. MacRobert. A Treatise on Bessel Functions. London: Macmillan, 1931.

Haselberg, K. V. and J. Krautkramer. Acustica 9, 359 (1959).

Huntington, H. B., A. G. Emslie, and V. W. Hughes. J. Franklin Institute 245, 1 (1948).

Kinsler, Lawrence E., Austin R. Frey, Alan B. Coppens, and James V. Sanders. Fundamentals of Acoustics. New York: John Wiley and Sons, Inc., 1982.

Krautkramer, J. and H. Krautkramer. Ultrasonic Testing of Materials. Berlin/Heidelberg, Germany: Springer Verlag, 1977.

Lord Rayleigh. The Theory of Sound. New York: Dover Publications, 1945, Vol. II.

Martin, F. D. and M. A. Breazeale. J. Acoust. Soc. Am. 49, 1668 (1971).

McSkimin, H. J. J. Acoust. Soc. Am. 22, 413 (1950).

Mercier, Noëlle. "Contrôle non destructif de matériaux par ultrasons." Chatillon, France: Office National D'Etudes et de Recherches Aérospatiales, 1974. Technical Report No. 232.

Papadakis, E. P. J. Acoust. Soc. Am. 42, 1045 (1967).

Papadakis, E. P. "Ultrasonic Diffraction from Single Apertures with Application to Pulse Measurements and Crystal Physics," pp. 151-211 in Physical Acoustics, Vol. XI, edited by W. P. Mason and R. N. Thurston. New York: Academic Press, 1975.

Rogers, Peter H. and A. L. Van Buren. J. Acoust. Soc. Am. 55, 724 (1974).

Rose, Joseph L. Br. J. Non-Destr. 17, 109 (1975)

Scott, Gerald W. "Amplitude and Phase of Rayleigh-Angle Reflections of Gaussian Ultrasonic Beams Incident on Liquid-Solid Interfaces," Master's thesis, The University of Tennessee, Knoxville, 1975.

Truell, Rohn, Charles Elbaum, and Bruce B. Chick. Ultrasonic Methods in Solid State Physics. New York: Academic Press, 1969.

Truell, Rohn and W. Oates. J. Acoust. Soc. Am. 35, 1382 (1963).

Williams, J. and J. Lamb. J. Acoust. Soc. Am. 30, 308 (1958).

APPENDICES

APPENDIX A

AN APPLICATION OF THE RECIPROCITY THEOREM

A. THE RECIPROCITY THEOREM

Let us assume two identical transducers 1 and 2. Let a volume V with closed surface S bound these two sources but not enclose them, as shown in Figure A-1. ϕ_1 is the velocity potential for transducer 1 and ϕ_2 for transducer 2. If we excite transducer 1 only, the description of the propagation of the wave in volume V is given by:

$$\nabla^2\phi_1 = -K^2\phi_1 \tag{A-1}$$

and the particle velocity $\vec{u}_1 = \nabla\phi_1$ and the pressure $P_1 = -j\omega\rho_0\phi_1$. Similarly, if we now excite transducer 2 only at the same frequency ω, we have:

$$\nabla^2\phi_2 = -K^2\phi_2 \tag{A-2}$$

and again, $\vec{u}_2 = \nabla\phi_2$ and $P_2 = j\omega\rho_0\phi_2$.

From Green's theorem:

$$\oint_S (\phi_1\nabla\phi_2 - \phi_2\nabla\phi_1) \cdot \hat{n}\, dS = \int_V (\phi_1\nabla^2\phi_2 - \phi_2\nabla^2\phi_1)dV \ . \tag{A-3}$$

Substituting (A-1) and (A-2) in (A-3) we have:

$$-j\omega\rho_0 \oint_S (P_1\,\vec{u}_2 - P_2\,\vec{u}_1) \cdot \hat{n}\, dS = \int_V (-\phi_1K^2\phi_2 + \phi_2K^2\phi_1)dV \ . \tag{A-4}$$

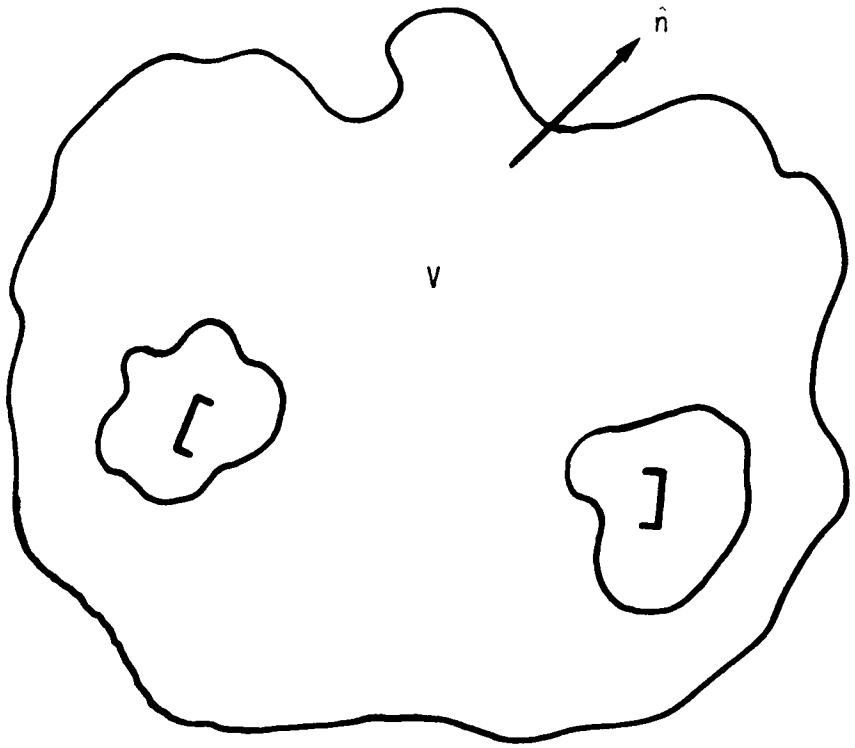


Figure A-1. Theoretical Position of Two Transducers Enclosed in a Volume V.

The right hand side of (A-5) vanishes identically and we have:

$$\oint_S (P_1 \vec{u}_2 - P_2 \vec{u}_1) \cdot \hat{n}\, dS = 0 .$$

This is the expression of the principle of reciprocity. Let us now restrict this theorem to the situation where the closed surface is made of an infinite rigid baffle of surface S_B such that $(\vec{u}\cdot\vec{n}) = 0$ on S_B. Then the only surface allowed to react to the pressure waves are the two transducer surfaces S_1 and S_2. Then, (A-5) becomes:

$$\int_{(S_1+S_2)} (P_1 \vec{u}_2 - P_2 \vec{u}_1) \cdot \hat{n}\, dS = 0 \qquad \text{(A-6)}$$

or equivalently,

$$\int_{S_2} P_1 \vec{u}_2 \cdot \hat{n}\, dS - \int_{S_2} P_2 \vec{u}_1 \cdot \hat{n}\, dS = \int_{S_1} P_2 \vec{u}_1 \cdot \hat{n}\, dS - \int_{S_1} P_1 \vec{u}_2 \cdot \hat{n}\, dS . \qquad \text{(A-7)}$$

Since the original assumption is that one transducer is passive while the other is active, then when one transducer is active the pressure over the surface of the second transducer is not zero but the velocity over that surface is zero. This means that the negative terms of Eq. (A-7) go to zero giving:

$$\int_{S_2} P_1 \vec{u}_2 \cdot \hat{n}\, dS = \int_{S_1} P_2 \vec{u}_1 \cdot \hat{n}\, dS . \qquad \text{(A-8)}$$

B. SMALL SOURCES IDENTITY

If the two sources 1 and 2 are small with respect to the wavelength and located several wavelengths apart such that the pressure is uniform over each source, then (A-8) when time is considered can be expressed as:

$$\frac{1}{P_1(t)} \int_{S_1} u_1(t) \cdot \hat{n}\, dS = \frac{1}{P_2(t)} \int_{S_2} \vec{u}_2(t) \cdot \hat{n}\, dS \,. \tag{A-9}$$

We now define the rate at which the volume, in the vicinity of the source, is displaced in function of the source strength Q as:

$$Q\, e^{j\omega t} = \int_S \vec{u}(t) \cdot \hat{n}\, dS \,. \tag{A-10}$$

Using the fact that the variation of P is given by $P_1(t) = P_1\, e^{j\omega t}$ and Eq. (A-10), we obtain from Eq. (A-9) that

$$\frac{Q_1}{P_1} = \frac{Q_2}{P_2} \,. \tag{A-11}$$

Therefore the ratio of source strength to pressure for a small source is independent of the shape of the source.

APPENDIX B

A COMPUTER PROGRAM FOR CORRECTING ULTRASONIC ATTENUATION DATA

```
C       THIS PROGRAM IS CODED IN FORTRAN10 LANGUAGE.
C       IT CORRECTS AMPLITUDE VALUES OBTAINED IN A WEDGED
C       SAMPLE WITH A CIRCULAR ULTRASONIC TRANSDUCER.
C       IT ALSO CALCULATES THE CORRECTED ATTENUATION
C       BETWEEN ECHO 1 AND N (N<15)
C
C
C       THE INPUT VARIABLES ARE:
C
C       V: VELOCITY OF THE WAVE IN THE SAMPLE (CM/USEC)
C       F: FREQUENCY (MHZ)
C       D: DIAMETER OF THE PIEZOELECTRIC ELEMENT (CM)
C       SL: SAMPLE LENGHT (CM)
C       GAMMA: WEDGE ANGLE (RADIANS)
C
C       THE OUTPUT VARIABLES ARE:
C
C       AXXX: AMPLITUDE
C       DBXXX: ATTENUATION (DECIBELS/CM)
C       WHERE XXX MEANS:
C                MP: UNCORRECTED
C                CD: DIFFRACTION CORRECTED
C                CDG: CORRECTED FOR DIFFRACTED WAVE GEOMETRY
C                CPG: CORRECTED FOR PLANE WAVE GEOMETRY
C
C
      IMPLICIT DOUBLE PRECISION (M)
      DIMENSION AMP(15),ACD(15),ACPG(15),ACDG(15)
      DIMENSION RMP(15),RCD(15),RCPG(15),RCDG(15)
      DIMENSION RC(15),ZC(15)
      COMMON PI,A,SL,GAM2N,WK,OMEGA,ALAMBD,ECHONO
      COMMON  ROO,ZO,S,SRF
      PI = 3.1415926
      V = 5.840E-1
10    READ  (1,120) F, D,SL,GAMMA
      A = D/2.
      IF (F.GT.100.0)         STOP
      ALAMBD = V/F
      OMEGA = 2.*PI*F
      WK = 2.*PI/ALAMBD
```

```
      WRITE (5,130)  A,SL,GAMMA,F
      ICOUNT=1
20    READ (1,140) AMP(ICOUNT)
      IF (AMP(ICOUNT).GT.100.0)                GO TO 30
      ICOUNT=ICOUNT+1
      GO TO 20
30    N = ICOUNT-1
      DO 90 I=1,N
      ECHONO = FLOAT(I)
      GAM2N = 2.0*GAMMA*ECHONO
      ZPAR = ECHONO*SL*2.0
      S = (ZPAR*ALAMBD)/((A)**2)
40    CALL   DIFCOR (CD)
      RDO = 0.0
      ZO = ZPAR
      ACD(I)=(AMP(I))/(CD)
      CALL FLUCTJ(HGAM2N)
      FARFLD = (D**2-ALAMBD**2)/(4*ALAMBD)
      IF(ZPAR.LT.(1.0*FARFLD))          GO TO 60
50    CALL   DSKCOR (CDG)
      ACDG(I) = AMP(I)/CDG
      RC(I) = RDO
      ZC(I) = ZO
      ZF = SQRT(RDO**2+ZO**2)/FARFLD
      IF (ZF.LT.3.0)          GO TO 70
      GO TO 80
60    ACDG(I) = ACD(I)
      ACPG(I)    = ACDG(I)/HGAM2N
      RC(I)      = 0.
      ZC(I)      = ZPAR
      GO TO 90
70    CONTINUE
C     WE NOW CORRECT THE FARFIELD APPROXIMATION TO IMPROVE
C     ITS CONVERGENCE.
      IF(ZF.LT.1.5)CF=(ZF-1.)*0.6+0.4
      IF(ZF.GT.1.5.AND.ZF.LT.2.)CF=(ZF-1.5)*0.4+0.7
      IF(ZF.GT.2.0.AND.ZF.LT.2.5)CF=(ZF-2.)*0.14+0.9
      IF(ZF.GT.2.5)CF=(ZF-2.5)*0.04+0.97
      ACDG(I) = ACDG(I)*CF
80    ACPG(I) = ACD(I)/HGAM2N
90    CONTINUE
      WRITE (5,150)
      DO 100 I = 1,N
      RMP(I) = AMP(I)/AMP(1)
      RCD(I)= ACD(I)/ACD(1)
      RCDG(I) = ACDG(I)/ACDG(1)
      RCPG(I)= ACPG(I)/ACPG(1)
      X=SQRT(RC(I)**2+ZC(I)**2)-SQRT(RC(1)**2+ZC(1)**2)
      WRITE (5,180) I,AMP(I),ACD(I),ACDG(I),ACPG(I)
      IF (I.EQ.1)          GO TO 100
```

```
      DBMP = 20.0*ALOG10(RMP(I))/X
      DBCD  =  20.0*ALOG10(RCD(I)) /X
      DBCDG = 20.0*ALOG10(RCDG(I)) /X
      DBCPG = 20.0*ALOG10(RCPG(I)) /X
      WRITE (5,170) DBMP,DBCD,DBCDG,DBCPG
100   CONTINUE
      GO TO 10
      RETURN
110   STOP
120   FORMAT (3F8,8X,E11.3)
130   FORMAT (1H1,4(1X,1PE13.5))
140   FORMAT ( F5)
150   FORMAT (1X,'THE RESULTS ARE GIVEN AS'/1X,'ECHO NUMBER
     1    AMP',16X,'ACD',16X,'ACDG',16X,'ACPG'/12X,'
     2    DBMP',15X,'DBCD',15X,'DBCDG',15X,'DBCPG')
160   FORMAT (1H-,'ECHO  1',1X,4(1PE16.9))
170   FORMAT (1HO,8X,4(1PE16.9))
180   FORMAT (1H-,'ECHO ',I2,1X,4(1PE16.9))
      END
C
C
      SUBROUTINE DIFCOR(CD)
C
C     THIS IS ROGERS AND VAN BUREN CORRECTION FOR DIFFRACTION
C
C
      IMPLICIT DOUBLE PRECISION (M)
      COMMON PI,A,SL,GAM2N,WK,OMEGA,ALAMBD,ECHONO
      COMMON  ROO,ZO,S,SRF
        MARG=2.*PI/S
C     CALL THE IMSL FUNCTIONS
      DJO = MMBSJO(MARG,IER)
      DJ1 = MMBSJ1(MARG,IER)
10    CD =SQRT((COS(MARG)-DJO)**2+(SIN(MARG)-DJ1)**2)
      RETURN
        END
C
C
      SUBROUTINE FLUCTU (HGAM2N)
C
C     THIS IS TRJELL AND OATES FLUCTUATION CORRECTION
C
C
      IMPLICIT DOUBLE PRECISION (M)
      COMMON PI,A,SL,GAM2N,WK,OMEGA,ALAMBD,ECHONO
      COMMON  ROO,ZO,S,SRF
      MARG = ABS(WK*A*SIN(GAM2N))
      HGAM2N = 1.0
      IF (MARG.LT.1.0D-8)                    GO TO 10
```

```
C       CALL THE IMSL  FUNCTION MMBSJ1
        DJ1 = MMBSJ1(MARG,IER)
        HGAM2N = ABS(2.0*DJ1/MARG)
10      CONTINUE
        RETURN
        END
C
C
        SUBROUTINE DSKCOR (CDG)
C
C       THIS IS THE DIFFRACTED WAVE GEOMETRY CORRECTION
C
C
        IMPLICIT DOUBLE PRECISION (M)
        COMMON PI,A,SL,GAM2N,WK,OMEGA,ALAMBD,ECHONO
        COMMON  ROO,ZO,S,SRF
        EXTERNAL FARP,FARPD
        ROO = ECHONO*SL*SIN(GAM2N)
        TAN = SIN(GAM2N/2.)/COS(GAM2N/2.)
        ZO  = 2.*ECHONO*SL-ROO*TAN
C
C       CALL THE IMSL NUMERICAL INTEGRATION FUNCTION DBLINT
C       WHERE FARP AND FARPD DEFINE THE PRESSURE AT A
C       POINT (R,THETA) LOCATED IN THE FARFIELD.
C
        R1 = 0.0
        R2 = A
        AERR = 1.0E-3
        THETA1 = 0.0
        THETA2 = 2.*PI
        C=DBLINT (FARP,R1,R2,THETA1,THETA2,AERR,ERROR,IER)
        CD=DBLINT(FARPD,R1,R2,THETA1,THETA2,AERR,ERROR,IER)
        SRF = PI*(A**2)
        CDG = SQRT((C/SRF)**2+(CD/SRF)**2)
        RETURN
        END
C
C
        REAL FUNCTION FARP (R,THETA)
        IMPLICIT DOUBLE PRECISION (M)
        COMMON PI,A,SL,GAM2N,WK,OMEGA,ALAMBD.ECHONO
        COMMON  ROO,ZO,S,SRF
        RO = ABS(SQRT(((ROO+R*COS(THETA)*COS(GAM2N)
        1)**2)+(R*SIN(THETA))**2))
        Z = ZO - R*COS(THETA)*SIN(GAM2N)
        DIR = 1.
        OROZ = SQRT(RO**2+Z**2)
        MARG = WK*A*RO/OROZ
        DJ1 = MMBSJ1(MARG,IER)
```

```
      IF(MARG.GT.1.D-8)DIR=2.*DJ1/MARG
      PAXIS=2*SIN((PI/ALAMBD)*(SQRT(A**2+OROZ**2)-OROZ))
      FARP = DIR*COS(WK*OROZ)*R*PAXIS
10    CONTINUE
      RETURN
      END
      REAL FUNCTION FARPD (R,THETA)
      IMPLICIT DOUBLE PRECISION (M)
      COMMON PI,A,SL,GAM2N,WK,OMEGA,ALAMBD,ECHOND
      COMMON  ROO,ZO,S,SRF
      RO = ABS(SQRT(((ROO+R*COS(THETA)*COS(GAM2N)
      1)**2)+(R*SIN(THETA))**2))
      Z = ZO - R*COS(THETA)*SIN(GAM2N)
      OROZ = SQRT(RO**2+Z**2)
      DIRD = 1.
      MARG = WK*A*RO/OROZ
      DJ1 = MMBSJ1(MARG,IER)
      IF(MARG.GT.1.D-8)DIRD=2.*DJ1/MARG
      PAXIS=2*SIN((PI/ALAMBD)*(SQRT(A**2+OROZ**2)-OROZ))
      FARPD = DIRD*SIN(WK*OROZ)*R*PAXIS
10    CONTINUE
      RETURN
      END
```

APPENDIX C

PHASE CORRECTION FOR VELOCITY MEASUREMENTS

As pointed out by many authors (McSkimin, 1950; Williams, 1958; Papadakis, 1967; Truell, 1969), when a wave is reflected from an interface a change of phase occurs. The phase shift is a function of the relative velocity, and the mechanical impedance of the two materials in contact at the interface as well as the frequency of the wave. This means that we have to correct for two interfaces: the sample-couplant interface and the couplant-crystal interface. However, as mentioned by Williams (1958) and Papadakis (1967), the effect of the bond material can be neglected when quartz crystals of frequency of 10 MHz or lower are wrung on the surface of a solid. Therefore, the only interface of concern here is the crystal-sample interface. A correction ΔT for the measured transit time T was given by Papadakis (1967) for a single transducer pulse echo overlap method which is very similar to the method used here. Neglecting the coupling layer, the condition for overlap gives

$$T \simeq 1/f_0$$

where f_0 is the resonance frequency and the correction for transit time in the bond is

$$\Delta T_1 \simeq \gamma_1/2\pi f_1$$

where γ_1 is the phase shift given in radians for frequency f_1. As pointed out by Williams (1958), the factor γ changes signs depending on whether the frequency f is higher or lower than the resonant frequency f_0. Furthermore, when the coupling layer is negligible, γ is proportional to the frequency. Therefore, by dividing the correction ΔT into two parts, one for frequencies higher than f_0 (ΔT_G) and one for frequencies lower than f_0 (ΔT_L) and taking the average ($\tilde{\Delta T}$) of both (since about the same number of minima were observed on both sides of f_0), a good indication of the magnitude of $\tilde{\Delta T}$ can be obtained. That is:

$$\tilde{\Delta T} = (\Delta T_L + \Delta T_H)/2$$

where

$$\Delta T_L = +\gamma_L/2\pi f_L$$
$$\Delta T_H = +\gamma_H/2\pi f_H$$

and

$$\gamma_H = +|2 \tan^{-1} a|$$
$$\gamma_L = -|2 \tan^{-1} a|$$

where

$$a \simeq \frac{z_t}{z_s} [\tan \theta_t] .$$

The factor z refers to the mechanical impedance and the indices t and s refer respectively to the transducer piezoelectric material[1] and the sample.[2] The factor θ_t is given by:

$$\theta_t = 2 \times \pi \times f \times \ell_t / v_t$$

where ℓ is the crystal thickness and v the velocity of propagation of the ultrasonic wave in the crystal.

Applying the correction, it was found that the time correction ΔT_L applied for the average low frequency f_L of the 21 sets of measurements was approximately -0.1%, whereas the correction of the time due to the frequencies higher than the center frequency ΔT_H, using the average high frequency f_H, was approximately +0.12%. The result of these two corrections is that they almost exactly compensated for each other and the average correction $\tilde{\Delta T}$ is about 50 times smaller than the standard deviation of the measurement.

The values of the parameters used are listed in Table C-1.

---

[1] The values of z_t, ℓ_t, and v_t were obtained from Krautkramer (1969).

[2] z_s was obtained by evaluating the density ρ_s of the sample and using the equation $z_s = v_s \times \rho_s$ where the previously uncorrected velocity $\tilde{v}$ was used as v_s.

TABLE C-1

PHASE CORRECTION DATA

$\tilde{f}_H$	= 4.550 MHz
$\tilde{f}_L$	= 3.580 MHz
f_0	= 4.003 MHz
z_t/z_s	= 0.3200
ℓ_t	= 0.07175 cm
v_t	= 0.56984 cm/μsec
γ_L	= -.2040
γ_H	= +.3038
T	= 8.5042 μsec
ΔT_L	= -9.069×10^{-3} μsec
ΔT_H	= $+10.626 \times 10^{-3}$ μsec
$\Delta\tilde{T}$	= 7.783×10^{-4} μsec
$\Delta\tilde{T}/T$	= 0.009%

APPENDIX D

THE RECEIVER DIRECTIVITY MODEL

The magnitude of the mechanical deformation of the piezoelectric element is dependent upon the distribution of the pressure vectors on the receiver surface. If one assumes that an infinite plane wave is impinging on the receiver, then the magnitude of the pressure deformation on the receiver $|P|_r$ can be related to the average maximum pressure of the wave $\tilde{P}$ by the use of a directivity function $H_r(\theta_i)$ where θ_i is the incidence angle:

$$|P|_r = \tilde{P}\, H_r(\theta_i) \ . \tag{D-1}$$

Kinsler et al. (1982) report different applications of the directivity function and show mathematically that the reciprocity theorem can be invoked to prove that the directivity factor of a receiver is given by the magnitude of the directivity function of the same vibrating element when used as a transmitter. A mathematical proof as applied to a plane wave propagation in shown here.

We now assume the sources 1 and 2, described in Appendix A, to be large compared to the wavelength and made of an active rigid piston located in an infinite rigid baffle such that:

$$\vec{u} \cdot \hat{n} = u \tag{D-2}$$

then Eq. (A-8) becomes

$$u_2 \langle (P)_1 \rangle_{S_2} (S_2) = u_1 \langle (P)_2 \rangle_{S_1} (S_1) \qquad \text{(D-3)}$$

where $\langle (P)_i \rangle_{S_j}$ means the pressure P integrated on the surface S_j when only the transducer i is active. Furthermore, we will assume that: the two transducer acoustic axes both make an angle θ with the wave coming from the other transducer; the distance R between the center of the two transducers is large enough that Fraunhofer diffraction conditions exist; and the ratio $\frac{S_j}{R}$ is so small that the wave originating on S_i appears plane when it reaches the transducer S_j. This is shown in Figure D-1. The pressure felt on element 2 due to the source 1 $\langle (P)_1 \rangle_{S_2}$ can be defined as a function of the pressure field of P_1 called $\langle P_1(R,\theta) \rangle_{S_2}$ where θ is the angle between the acoustic axes. Since we have plane waves, then this pressure field is constant over the surface S_2. Then:

$$\langle P_1(R,\theta) \rangle_{S_2} = P_1(\theta) \times A(R) \qquad \text{(D-4)}$$

where A(R) is a pressure amplitude function. Similarly

$$\langle (P)_2 \rangle_{S_1} = P_2(\theta) \times A(R) \; . \qquad \text{(D-5)}$$

Replacing (D-4) and (D-5) in (D-3) gives

$$A(R)\, u_2\, P_1(\theta)\, S_2 = A(R)\, u_1\, P_2(\theta)\, S_1 \; . \qquad \text{(D-6)}$$

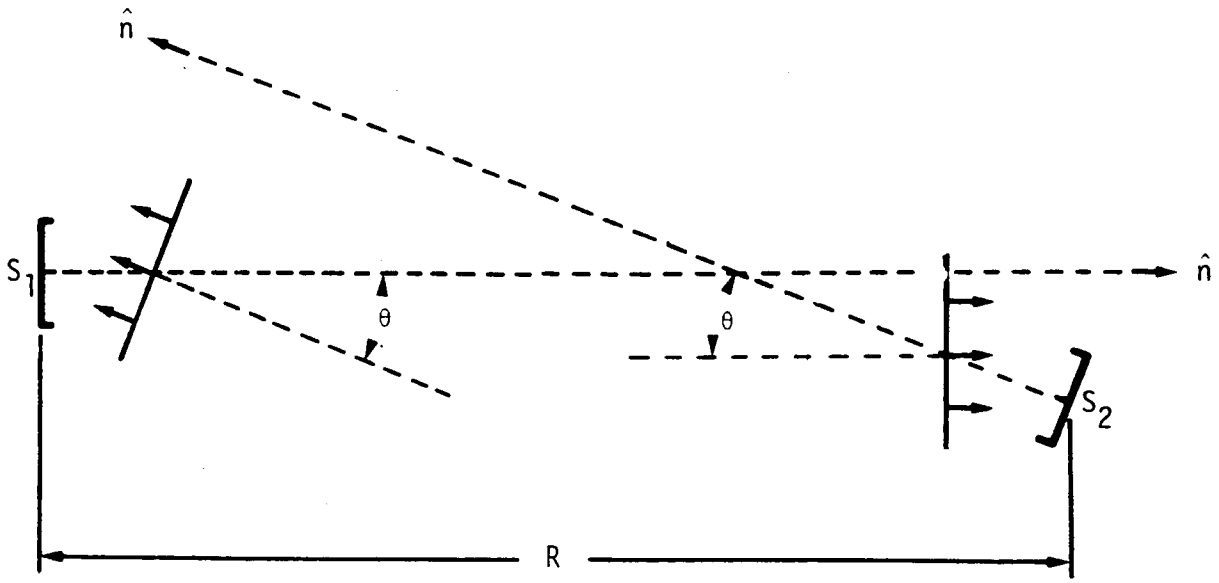


Figure D-1. Schematic Showing the Relative Position of the Transducers S_1 and S_2 and the Incident Angle θ of the Incoming Plane Wave.

In Figure D-2 both acoustic axes of the two transducers are coincident, then (D-6) transforms to:

$$A(R)\ u_2\ P_{1_{axis}}\ A_2 = A(R)\ u_1\ P_{2_{axis}}\ A_1\ . \tag{D-7}$$

The magnitude of the ratio of (A-16) over (A-17) gives

$$\left|\frac{P_1(\theta,t)}{P_{1_{axis}}}\right| = \left|\frac{P_2(\theta,t)}{P_{2_{axis}}}\right|\ . \tag{D-8}$$

If we now define a directivity factor $H_i(\theta)$ as

$$H_i(\theta) = \left|\frac{P_i(\theta)}{P_{i_{axis}}}\right|\ , \tag{D-9}$$

then replacing (A-18) in (A-19) we have

$$H_1(\theta) = H_2(\theta)\ . \tag{D-10}$$

Since this equation must be true independent of which transducer is a transmitter and which is a receiver, and since both transducers are identical, then we must conclude that the receiver directivity factor $H(\theta)$ is the same as the transmitter directivity factor.

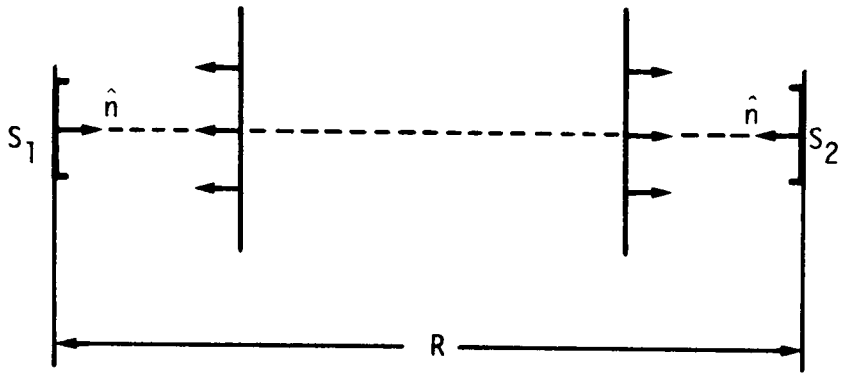


Figure D-2. Schematic Showing the Relation between Two Transducers S_1 and S_2 which Have Parallel Acoustic Axes.

APPENDIX E

THE GAUSSIAN TRANSDUCER

Let us assume that a pressure disturbance has a Gaussian form described by the relation:

$$P(\rho,0) = P_0 \, e^{-\rho^2/T_0^2} \tag{E-1}$$

where ρ is the radial coordinate of a cylindrical coordinate system originating at the center of the source. T_0 is the radius for which the amplitude decreases to 1/e of its maximum value. Now, let this disturbance propagate in a lossless fluid a distance z. Since the Fourier transform of a Gaussian distribution is a Gaussian distribution the pressure $P(\rho,z)$ should have the form of Eq. (E-1).

$$P(\rho,z) = P(z) \, e^{-\rho^2/T^2(z)} \tag{E-2}$$

Then from the principle of conservation of energy:

$$\int_0^\infty P(\rho,0) = \int_0^\infty P(\rho,z) \ , \tag{E-3}$$

or equivalently,

$$\int_0^\infty P_0 \, e^{-\rho^2/T_0^2} \, d\rho = \int_0^\infty P_z \, e^{-\rho^2/T^2(z)} \, d\rho \tag{E-4}$$

where P_z is the pressure on the axis of propagation at a distance z from the origin. Equivalently then,

$$\frac{P_0}{P_z} = \frac{\int_0^\infty e^{-\rho^2/T^2(z)}\, d\rho}{\int_0^\infty e^{-\rho^2/T_0^2}\, d\rho} . \qquad \text{(E-5)}$$

From Abramowitz (1972):

$$\int_0^\infty e^{-\rho^2/T^2} d\rho = T\sqrt{\pi}/2 . \qquad \text{(E-6)}$$

Then replacing (E-6) in (E-5)

$$\frac{P_0}{P_z} = \frac{T(z)}{T_0} . \qquad \text{(E-7)}$$

From Haselberg and Krautkramer (1959):

$$P_z = P_0/\phi(z) \qquad \text{(E-8)}$$

where $\phi(z) = [(z\lambda/\pi T_0^2)^2 + 1]^{1/2}$. Then replacing (E-8) in (E-7):

$$T(z) = \phi(z)\, T_0 . \qquad \text{(E-9)}$$

Replacing (E-9) and (E-8) in (E-2) we obtain:

$$P(\rho,z) = \frac{P_0}{\phi(z)} e^{-\rho^2/\phi^2(z)T_0^2} \qquad \text{(E-10)}$$

We now assume a plane wave propagation.[1] Then

$$P(\rho,z,t) = \frac{P_0}{\phi(z)} e^{-\rho^2/\phi^2(z)T_0^2} e^{i(\omega t-kz)} . \qquad \text{(E-11)}$$

w the magnitude of the average pressure on the receiver is obtained by integration of (E-11):

$$|\tilde{P}(z)| = \frac{P_0}{\rho} \int_s \frac{e^{-\rho^2/\phi^2(z)T_0^2}}{\phi(z)} e^{-kz} ds . \qquad \text{(E-12)}$$

Following the same process described in Chapter II we will apply this unidirectional wave propagation model to a multiply reflected wave. We now assume that the dimension of the receiver in the y direction is small enough that the amplitude does not vary significantly along the y dimension of the receiver. Then Eq. (E-12) becomes:

$$|\tilde{P}(z)| = \frac{P_0}{\Delta x} \int_{\Delta x} \frac{e^{-\rho(x)^2/\phi^2(z(x))T_0^2}}{d(z(x))} e^{-ikz(x)} dx \qquad \text{(E-13)}$$

where Δx is the length of the receiver electrode. Now we replace the value of $z(x)$ and $\rho(x)$ by the coordinate system developed in Chapter II. Then

$$|\tilde{P}(z)|_n = \frac{P_0}{\Delta x} \int_{-\Delta x/2}^{\Delta x/2} e^{-(x\cos(\gamma_n)-\rho(0,0)_n)^2/\phi^2(z(0,0)_n+x\sin(\gamma_n))}$$

$$\times \frac{1}{\phi(z(0,0)_n + x\sin(\gamma_n))} e^{-ik(z(0,0)_n+x\sin(\gamma_n))} dx . \qquad \text{(E-14)}$$

---

[1] According to Haselberg and Krautkramer (1959) this introduces an error on P smaller than e^{-a^2/T_0^2} where a is the radius of the piezoelectric element.

We now approximate $\phi(z(0,0)n + x\sin(\gamma_n)$ by $\phi(z(0,0)n)$.[1] Then (E-14) becomes

$$|\tilde{P}(z)| = \frac{P_0}{\Delta x\ \phi(z(0,0)n)} \int_{-\Delta x/2}^{\Delta x/2} e^{-x^2(\cos^2(\gamma_n)/\phi^2(z(0,0)n))}$$
$$e^{-x(i\sin(\gamma_n)-2\cos(\gamma_n)\rho(0,0)n/\phi^2(z(0,0)n))}$$
$$e^{-(ikz(0,0)n+\rho^2(0,0)n)}dx \ . \qquad \text{(E-15)}$$

From Abramowitz (1972):

$$\int e^{-(Ax^2+2Bx+C)} = 1/2\sqrt{\frac{\pi}{A}}\, e^{\frac{B^2-AC}{A}}\, \mathrm{erf}(\sqrt{A}x + \frac{B}{\sqrt{A}}) \ . \qquad \text{(E-16)}$$

Then (E-15) becomes

$$|\tilde{P}(\Delta z)| = \frac{P_0\ \sqrt{\pi}}{2\Delta x\ \phi(z(0,0)n)\sqrt{A}}\, e^{\frac{B^2-AC}{A}}$$
$$\times\ \mathrm{erf}(\sqrt{A}\ x + \frac{B}{\sqrt{A}}) \Big|_{-\Delta x/2}^{\Delta x/2} \qquad \text{(E-17)}$$

where

$$A = \cos^2(\gamma_n)/\phi^2(z(0,0)_n)$$

$$B = \frac{i\ \sin(\gamma_n)\ -\ 2\cos(\gamma_n)\rho(0,0)_n/\phi^2(z(0,0)_n}{2}$$

$$C = ikz(0,0)_n + \rho^2(0,0)_n \ .$$

---

[1] This approximation for a steel sample, at a frequency of 4 MHz, and for $\gamma = 7.45 \times 10^{-3}$, was calculated to introduce an error of less than 1.5% on the pressure value for n = 1 and the error decreases as n increases.

The circular piezoelectric element and the mechanical coupling technique described in Chapter III are also used with the Gaussian transducer. The main difference between the Gaussian transducer and the previously described transducer is that now the source electrode is a rectangular strip of aluminum wrung onto this piezoelectric element. By positioning the circular piezoelectric element such that the rectangular source electrode has its length normal to the slope of the face it is then possible to use two smaller rectangular electrodes as receiver by placing them on either side of the source electrode such that the pattern of electrodes looks like a cross. Then the displacement and rotation of the propagating wave which occurs strictly in the $\rho_n' z_n'$ plane can be handled by means of the cartesian coordinates as described above.

VITA

Serge Boudreault, son of Léon Boudreault and Marguerite Girard, is the oldest of a family of eight children. He was born in the city of Jonquière, Province of Québec, Canada, on October 16, 1952. In 1971 he graduated from the Collège D'Enseignement Général et Professionel de Jonquière, majoring in Pure and Applied Science. In 1972 he joined the Canadian Armed Forces Regular Officer Training Plan and in 1974 obtained a Bachelor of Engineering degree from L'Université Du Québec a Chicoutimi, majoring in geological engineering. In 1975 he graduated as a Lieutenant from the Canadian Forces School of Land Ordnance and Aerospace Engineering. He was then posted to Canadian Forces Base Bagotville where he served for one year as Base Flight Maintenance Officer and for another year as Armament and Photo Officer. In June 1977 he was posted to the Canadian Forces School of Land Ordnance and Aerospace Engineering to serve as an instructor in the Aerospace Engineer Training Company. In December 1977 he was promoted to Captain. He was selected in 1980 for advance training in Nondestructive Testing at The University of Tennessee, Knoxville, Tennessee. Subsequent to his graduation from the Master of Science program, he will hold the position of Nondestructive Testing Officer at the Aerospace Maintenance Development Unit at Canadian Forces Base Trenton, Trenton, Ontario, Canada.

He is married to Lyne Dallaire, also from Jonquière, and has two children: Isabelle (4 years) and Sébastien (6 months).